

Mechanism and modelling of the secondary baroclinic vorticity in the Richtmyer–Meshkov instability

Naifu Peng^{1,2}, Yue Yang^{1,2,3,†}, Jinxin Wu¹ and Zuoli Xiao^{1,2,3}

¹State Key Laboratory for Turbulence and Complex Systems, College of Engineering, Peking University, Beijing 100871, PR China

²Center for Applied Physics and Technology and HEDPS, Peking University, Beijing 100871, PR China

³Beijing Innovation Center for Engineering Science and Advanced Technology, Peking University, Beijing 100871, PR China

(Received 16 February 2020; revised 21 September 2020; accepted 30 November 2020)

We elucidate the effect of the secondary baroclinic vorticity (SBV) on the Richtmyer–Meshkov instability (RMI) accelerated by a weak incident shock and develop a vortex-based model for spike and bubble growth rates. Two major mechanisms of the single-mode RMI, the primary baroclinic vorticity (PBV) and the pressure perturbation, are distinguished by simplified models with the vortex-surface field. We find that the effect of the pressure perturbation can be neglected in the present RMI, and the growth of the interface or vortex surface is first driven by the PBV. Subsequently, the SBV, generated by the misalignment between the density gradient across the interface and the pressure gradient produced by the PBV-induced velocity, leads to the nonlinear growth of the interface with the generation of spikes and bubbles. Inspired by this mechanism, we develop a predictive model of spike and bubble growth rates using the motion of viscous vortex rings. The circulation of the vortex ring is modelled with the SBV effect. This model is validated by five data sets of direct numerical simulations and experiments of the single-mode RMI with various initial conditions.

Key words: vortex dynamics, shock waves

1. Introduction

The Richtmyer–Meshkov instability (RMI) is initiated when a shock wave impacts on a perturbed interface between two fluids of different densities (Richtmyer 1960; Meshkov 1969). The RMI is of importance for the supernova explosion (e.g. Arnett *et al.* 1989; Arnett 2000; Almgren *et al.* 2006), ignition in inertial confinement fusion (e.g. Lindl,

† Email address for correspondence: yyg@pku.edu.cn

McCrory & Campbell 1992; Taccetti *et al.* 2005; Aglitskiy *et al.* 2010) and combustion in scramjet engines (e.g. Yang, Kubota & Zukoski 1993; Khokhlov, Oran & Thomas 1999).

The RMI is generally explained by two mechanisms (see Brouillette 2002): (i) the primary baroclinic vorticity (PBV) generated by the misalignment of the shock pressure gradient and the interfacial density gradient, and (ii) pressure perturbations behind distorted transmitted and reflected waves. These two mechanisms, however, are still coupled in some extent, e.g. the pressure perturbations can modify the baroclinic vorticity (Fraleley 1986). Furthermore, most previous studies on the pressure perturbations (e.g. Ishizaki *et al.* 1996; Wouchuk & Nishihara 1997; Goncharov 1999; Velikovich *et al.* 2000; Wouchuk 2001) are based on the pressure perturbation equation (Richtmyer 1960; Zaidel 1960; Briscoe & Kovitz 1968) derived from linearized Navier–Stokes (known as NS) equations using asymptotic analysis. They cannot distinguish the effects from the distorted waves and the vorticity-induced velocity on the pressure perturbations, and they are restricted to the linear growth rate. As a result, the mechanisms controlling the nonlinear growth of the interface, in particular, the generation of spikes and bubbles (see Brouillette 2002), have not been elucidated.

The PBV is generated as the shock impacting on the interface, and its effects on the RMI have been extensively investigated (see Zabusky 1999; Zhou 2017*a,b*). Subsequently, the secondary baroclinic vorticity (SBV) was reported to be produced by the interaction of the interface and reflected waves (e.g. Zabusky & Zeng 1998; Zabusky & Zhang 2002; Zhang & Zabusky 2003) or the interaction of the interface and vortex-induced velocity. The latter type of the SBV was first found in the Kelvin–Helmholtz instability in stratified shear layers (e.g. Soteriou & Ghoniem 1995; Staquet 1995; Reinaud, Joly & Chassaing 2000), so its effects on the RMI were often mentioned in the late stage, particularly during the roll-up of the interface. Zabusky *et al.* (2003) found that this SBV dominates after the interface becomes multivalued and produces a negative circulation in a two-dimensional RMI. Peng, Zabusky & Zhang (2003) quantified this SBV effect and found that the SBVs with opposite signs are generated near the roll-up spike region and produce very unstable vortex bi-layers. These SBV effects were also found in the interaction of the shock with gas cylinders (e.g. Gupta, Zhang & Zabusky 2003; Vorobieff *et al.* 2004; Zhang *et al.* 2004) or the curtain-shaped interface (e.g. Zhang, Peng & Zabusky 2005). On the other hand, since the magnitude of SBV is much smaller than that of PBV, the SBV effects were usually neglected in the early stage of the RMI. We remark that the PBV may not directly lead to the asymmetric interfacial growth, e.g. the shock impacting on a symmetric interface may only generate the symmetric PBV, so the relatively small, vortex-induced SBV can still play an important role in generating the asymmetric spike and bubble at early times.

The nonlinear growth of the interface with spikes and bubbles, which occurs after a short linear growth (e.g. Richtmyer 1960; Fraley 1986; Ortega *et al.* 2010), is a key feature of the RMI. The perturbation analysis (see Haan 1991; Zhang & Sohn 1996; Vandenboomgaerde, Gauthier & Mügler 2002; Velikovich, Herrmann & Abarzhi 2014) found that the perturbation parameter with the density difference between the interface leads to a second-order term in the perturbation expansion, which is further linked to the asymmetric interfacial growth. A number of nonlinear models have been developed to predict the growth rates of spikes and bubbles. Zhang & Sohn (1997) derived a weakly nonlinear model by asymptotic expansions to the fourth-order term with the Padé approximation. This model was firstly for the two-dimensional RMI, and later extended to three dimensions (Zhang & Sohn 1999) and improved using higher-order approximations (Vandenboomgaerde *et al.* 2002). These weakly nonlinear models agree with experimental data at earlier times, but gradually deviate from the data at later times (see Niederhaus & Jacobs 2003; Jacobs & Krivets 2005). In the late stage, Alon *et al.* (1995) gave an

asymptotic power law of spike and bubble growth rates with time. Then several models were developed to match the growth rates from the weakly nonlinear models at early times and the power law at late times (e.g. Sadot *et al.* 1998; Mikaelian 2003; Dimonte & Ramaprabhu 2010; Luo, Wang & Si 2013), but this matching usually relies on empirical functions and parameters and lacks physical interpretations.

Since the PBV is deposited at the interface, it is natural to model the growth rates from vortex dynamics, which appears to involve more flow physics than the asymptotic models. Jacobs & Sheeley (1996) approximated the growth rate of the two-dimensional RMI by the induced velocity of two rows of positive and negative line vortices, which was restricted to the vanishing Atwood number A with a constant velocity circulation estimated by the initial growth rate. This model was extended to incorporate the effect of A using the time-varying circulation obtained from the direct numerical simulation (DNS) (Peng *et al.* 2003) or introducing an empirical perturbed vortex spacing (Likhachev & Jacobs 2005). On the other hand, the two-dimensional vortex-based models cannot estimate spike and bubble growth rates related to different time-varying circulations, and they can be inaccurate in predicting growth rates in the three-dimensional RMI (Chapman & Jacobs 2006) in which the motion of vortex rings should be considered.

In the present study for the three-dimensional RMI arising from a single-mode light/heavy interface accelerated by a weak planar shock, we distinguish the effects of the density difference, the PBV and the pressure perturbation on the RMI by developing a series of simplified models. With the aid of the vortex-surface field (VSF), a Lagrangian-based structure identification method developed by Yang & Pullin (2010), we characterize the asymmetric evolution of the vortex surface (VS) coinciding with the interface, and elucidate the mechanism of the SBV in the generation of spikes and bubbles. Inspired by the dynamics of the VS, we develop a predictive model for the nonlinear growth rates of spikes and bubbles based on the motion of viscous vortex rings with the SBV effect.

The outline of this paper is as follows. The DNS set-up of the single-mode RMI is described in § 2. We determine the PBV and introduce the VSF framework in the RMI in § 3, and elucidate the mechanism of the SBV in the nonlinear growth of the RMI in § 4. Then we develop a vortex-based model of spike and bubble growth rates, and validate the model using various DNS or experimental data sets in § 5. Some conclusions are drawn in § 6.

2. Simulation overview

2.1. Governing equations

The three-dimensional RMI is governed by the multicomponent Navier–Stokes equations in the conservative form (Kawai & Lele 2008; Tritschler *et al.* 2014):

$$\frac{\partial \rho}{\partial t} + \nabla \cdot (\rho \mathbf{u}) = 0, \quad (2.1)$$

$$\frac{\partial (\rho \mathbf{u})}{\partial t} + \nabla \cdot (\rho \mathbf{u} \mathbf{u} + p \mathbf{I} - \boldsymbol{\tau}) = 0, \quad (2.2)$$

$$\frac{\partial E}{\partial t} + \nabla \cdot [E \mathbf{u} + (p \mathbf{I} - \boldsymbol{\tau}) \cdot \mathbf{u} + \mathbf{q}_c + \mathbf{q}_d] = 0, \quad (2.3)$$

$$\frac{\partial (\rho Y_i)}{\partial t} + \nabla \cdot (\rho \mathbf{u} Y_i) - \nabla \cdot \mathbf{J}_i = 0. \quad (2.4)$$

Here, ρ denotes the mixture density, $\mathbf{u} = u_x \mathbf{i} + u_y \mathbf{j} + u_z \mathbf{k}$ the velocity, p the pressure and \mathbf{I} the identity tensor, where \mathbf{i} , \mathbf{j} and \mathbf{k} are unit vectors in the x -, y - and z -directions, respectively. Equations (2.1)–(2.4) are closed with the equation of state for ideal gas

$$p = \rho \frac{\mathcal{R}}{\bar{M}} T = (\bar{\gamma} - 1) \rho e, \quad (2.5)$$

where \mathcal{R} is the ideal gas constant, \bar{M} the molar mass, T the temperature, $\bar{\gamma}$ the ratio of specific heat capacities of the mixture and e the internal energy with

$$\rho e = E - \frac{1}{2} \rho \mathbf{u} \cdot \mathbf{u}. \quad (2.6)$$

In (2.2) and (2.3), the viscous stress tensor

$$\boldsymbol{\tau} = 2\bar{\mu} \mathbf{S} - \frac{2}{3} \bar{\mu} (\nabla \cdot \mathbf{u}) \mathbf{I} \quad (2.7)$$

for a Newtonian fluid obeys Stokes' hypothesis (see Graves & Argrow 1999), where $\bar{\mu}$ is the mixture viscosity, $\mathbf{S} = [\nabla \mathbf{u} + (\nabla \mathbf{u})^T]/2$ the strain-rate tensor and E the total energy per unit volume. In (2.4), Y_i is the mass fraction of species i with $i = 1, 2$ and $Y_1 = 1 - Y_2$ for two fluids. In (2.3), the heat flux is estimated by Fourier's law

$$\mathbf{q}_c = -\bar{\kappa} \nabla T \quad (2.8)$$

with the mixture heat conductivity $\bar{\kappa}$. Moreover, the effect of the enthalpy diffusion flux is incorporated using the interspecies diffusional heat flux (Cook 2009)

$$\mathbf{q}_d = \sum_{i=1}^2 h_i \mathbf{J}_i \quad (2.9)$$

with

$$\mathbf{J}_i = -\rho \left(D_i \nabla Y_i - Y_i \sum_{j=1}^2 D_j \nabla Y_j \right), \quad (2.10)$$

where h_i and D_i are, respectively, the enthalpy and the effective binary diffusion coefficient of species i . For each species, the viscosity μ_i is calculated by the Chapman–Enskog model (see Chapman & Cowling 1990) and D_i is approximated by the model in Ramshaw (1990). Then the multicomponent/molecular mixing rules are applied to obtain \bar{M} , $\bar{\gamma}$, $\bar{\mu}$ and $\bar{\kappa}$ (see Reid, Pransuitz & Poling 1987). Calculation of these parameters are detailed in appendix A in Tritschler *et al.* (2014).

2.2. Initial and boundary conditions

The RMI is simulated in a shock tube in the domain Ω within $0 \leq x, y \leq L$ and $-L \leq z \leq L$. It arises from a weak planar shock wave travelling from a light fluid with ρ_1 to a heavy fluid with ρ_2 and accelerating the interface between the two fluids. The quantities with subscript 1 or 2 denote those on the light or heavy fluid side, respectively. The single-mode perturbation

$$\varphi_I(\mathbf{x}) = \frac{z}{a_0} - \cos(kx) \cos(ky) = 0 \quad (2.11)$$

is imposed on the interface with the amplitude a_0 , wavenumber $k = 2\pi/\lambda$ and wavelength $\lambda = L$.

The incident shock, initially at $z = -L/2$, travels along the z -direction at the shock Mach number M_S . The initial preshock state is given by the stagnation pressure p_0 and temperature T_0 in quiescent fluids, and the density is set to $\rho_i = p_0 M_i / (\mathcal{R} T_0)$ with the species molar mass M_i . The post-shock density

$$\rho_S = \frac{(\bar{\gamma} + 1) M_S^2}{2 + (\bar{\gamma} - 1) M_S^2} \rho_1, \quad (2.12)$$

pressure

$$p_S = \frac{2\bar{\gamma} M_S^2 - \bar{\gamma} + 1}{\bar{\gamma} + 1} p_0 \quad (2.13)$$

and velocity $U_S = U_S \mathbf{k}$ with

$$U_S = \frac{2(M_S^2 - 1)}{(\gamma_1 + 1) M_S} \sqrt{\frac{\gamma_1 p_0}{\rho_1}} \quad (2.14)$$

are calculated by the Rankine–Hugoniot (known as RH) conditions (see Courant & Friedrichs 1999), and the post-shock temperature $T_S = p_S M_1 / (\rho_S \mathcal{R})$ is calculated from (2.5).

Initial distributions of the density, pressure, temperature and velocity in the shock tube are sketched in figure 1. They are given by

$$\rho(\mathbf{x}, t = 0) = (\rho_2 - \rho_1) \mathcal{H}(\varphi_I) - (\rho_S - \rho_1) \mathcal{H}(z/L + 1/2) + \rho_S, \quad (2.15)$$

$$\mathbf{u}(\mathbf{x}, t = 0) = [1 - \mathcal{H}(z/L + 1/2)] U_S \mathbf{k}, \quad (2.16)$$

$$p(\mathbf{x}, t = 0) = -(p_S - p_0) \mathcal{H}(z/L + 1/2) + p_S, \quad (2.17)$$

$$T(\mathbf{x}, t = 0) = -(T_S - T_0) \mathcal{H}(z/L + 1/2) + T_S, \quad (2.18)$$

$$Y_1(\mathbf{x}, t = 0) = 1 - \mathcal{H}(\varphi_I), \quad (2.19)$$

where \mathcal{H} denotes the Heaviside function. In the shock tube, periodic boundary conditions are applied in the x - and y -directions, and the Riemann boundary condition is used in the z -direction (see § II.A in Liu & Xiao 2016).

2.3. DNS

In the present DNS, the density interface is formed by the contact of air (light) and SF₆ (heavy). The Atwood number $A = (\rho_2 - \rho_1) / (\rho_1 + \rho_2)$ for the air–SF₆ interface is $A = 0.67$ with $M_1 = 28.964 \text{ g mol}^{-1}$ and $M_2 = 146.057 \text{ g mol}^{-1}$. In order to study the effects of A , we artificially vary the molar mass of the heavy fluid, as $M_2 = 53.7903 \text{ g mol}^{-1}$ and $260.676 \text{ g mol}^{-1}$, for additional two DNS cases at $A = 0.30$ and 0.80 , respectively.

We set $L = 0.1 \text{ m}$, $a_0 = 4 \times 10^{-3} \text{ m}$, $p_0 = 101.3 \text{ kPa}$, $T_0 = 293 \text{ K}$ and a low shock Mach number $M_S = 1.1$ without reshock. To keep the interface in the middle of Ω during the evolution, the initial velocity in the z -direction is subtracted by U_0^+ to offset the interface translation driven by the shock, where U_0^+ denotes the post-shock speed of the interface (Yang, Zhang & Sharp 1994) with the superscript ‘+’ for a post-shock quantity.

The DNS for solving (2.1)–(2.4) is carried out by the high-order turbulence solver (HOTS) developed by Liu & Xiao (2016). The HOTS is based on the high-order compact difference scheme with localized artificial diffusivity (known as LAD) (see Shankar, Kawai & Lele 2011; Olson & Lele 2013) and parallelized with the

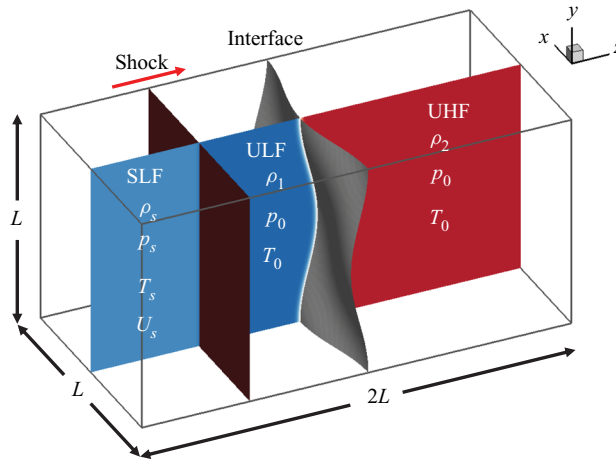


Figure 1. Schematic diagram of the initial distribution of the shocked light fluid (SLF), unshocked light fluid (ULF) and unshocked heavy fluid (UHF) with the shock and interface in the shock tube. The symmetry plane in the x -direction is colour-coded by $\rho_1 \leq \rho \leq \rho_2$ from blue through white to red.

A	U_0^+ (m s ⁻¹)	\dot{a}_0 (m s ⁻¹)	Z_0 (m)	Δt (s)
0.30	49.35	4.98	0	8×10^{-7}
0.67	36.22	8.50	0.025	1×10^{-6}
0.80	29.56	8.23	0.040	8×10^{-7}

Table 1. Parameters in three DNS cases.

message-passing interface. The spatial derivatives in (2.1)–(2.4) and the gradient terms in (2.8) and (2.10), are evaluated using a sixth-order compact finite difference scheme with the artificial diffusivity added near the shock and interface, and the temporal integration is marched by the third-order total-variation-diminishing (known as TVD) Runge–Kutta scheme (Gottlieb & Shu 1998). The HOTS has been validated to be stable and reasonably accurate for DNS of the RMI at $M_S \leq 1.6$, in which the localized artificial diffusivity does not affect the high accuracy of the numerical results for the interfacial mixing (see Liu & Xiao 2016; Wu, Liu & Xiao 2019).

The computational domain Ω is discretized by uniform grid points $N^2 \times 2N$ with the mesh spacing $\Delta x = L/N \approx 3.91 \times 10^{-4}$ m and $N = 256$. Two long sponge layers with non-uniform coarse grids are added at $z < -L$ and $z > L$ to avoid the effect of reflected waves at the outlet boundary in the z -direction (see Liu & Xiao 2016). For the finite thickness of the interface and shock, the Heaviside function in (2.15)–(2.19) is approximated by

$$\mathcal{H}(\alpha) = \frac{1}{2} \left[\operatorname{erf} \left(\frac{\alpha}{2\delta_0} \right) + 1 \right] \quad (2.20)$$

with the initial thickness $\delta_0 = 4 \times 10^{-4}$ m. The time period for the DNS is from $t = 0$ to $t = 0.032$ s with the time stepping Δt satisfying the Courant–Friedrichs–Lewy condition. Additionally, the initial interface location is shifted to $z = Z_0$ to avoid the long spikes moving out of Ω . The DNS parameters for the three cases are listed in table 1.

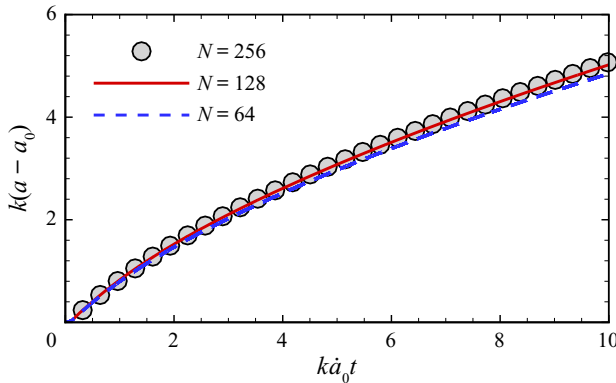


Figure 2. Temporal evolution of the scaled amplitude variation in the DNS grid convergence test at $A = 0.8$.

We conducted a convergence test for the case at $A = 0.8$ with $N = 64, 128$ and 256 . Figure 2 plots the evolution of the scaled amplitude variation $k(a - a_0)$ with the dimensionless time $k\dot{a}_0 t$, and its profiles with various N converge at $N = 256$. Furthermore, the baroclinic term in (3.10), which will be investigated in detail, is well-resolved for $N = 256$ in our convergence test (not shown). Hence, the resolution $N = 256$ is used in the present study.

Here, the amplitude $a(t) = [a_s(t) + a_b(t)]/2$ (see Brouillette 2002) of the interfacial perturbation is the average of the spike amplitude $a_s(t)$ and bubble amplitude $a_b(t)$. Referencing to the calculation of the mixing width (e.g. Thornber *et al.* 2010; Oggian *et al.* 2015), we calculate the spike and bubble amplitudes by integrating the mass fractions as

$$a_s(t) = \int_{-L}^L Y_2(x = 0, y = L/2, z, t) dz - L + Z_I(t) \tag{2.21}$$

and

$$a_b(t) = \int_{-L}^L Y_1(x = 0, y = 0, z, t) dz - L - Z_I(t), \tag{2.22}$$

respectively, with $a_s(0) = a_b(0) = a_0$. Both $a_s(t)$ and $a_b(t)$ depend on the location of the mean interface plane $Z_I(t)$ which is estimated by the interfacial location from the simulation with $a_0 = 0$ (see Long *et al.* 2009). Then the spike or bubble growth rate $\dot{a}_{s/b}(t)$ is the temporal derivative of $a_{s/b}(t)$, where the subscript ‘s/b’ denotes the quantity for spikes (s) or bubbles (b). The initial growth rate $\dot{a}_0 = \dot{a}_s(0) = \dot{a}_b(0)$ is calculated from the initial DNS result at various A and listed in table 1, and \dot{a}_0 will be useful in further modelling in § 5. It is noted that, although \dot{a}_0 can be approximated using the impulsive model of Richtmyer (1960), the reduction factor in this model can vary significantly with different initial conditions (see Liang *et al.* 2019).

3. PVB

3.1. Density and pressure distributions as the shock accelerating the interface

When the shock accelerates on the perturbed interface, complex waves are generated, along with significant density and pressure variations in Ω . Figure 3 sketches three stages of the accelerating process. The shock, located at $z = c(t)$, $-L \leq c(t) \leq L$, first touches the interfacial trough at $z = -a_0$ and $t = t_I$, and then moves away from the interfacial

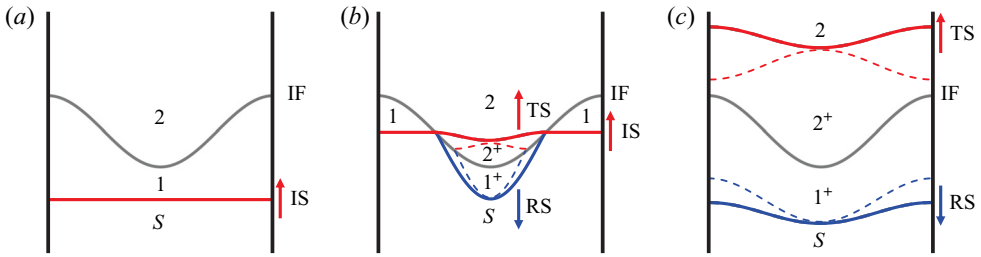


Figure 3. Schematic diagram for the interaction between the shock and the interface (IF): (a) before the incident shock (IS) accelerating the interface; (b) during the shock accelerating the interface, when a part of the incident shock becomes the transmitted shock (TS) and reflected shock (RS) is generated; (c) after the shock accelerating the interface. Dash lines denote transverse waves behind transmitted and reflected shocks.

crest at $z = a_0$ and $t = t_I + \delta t_I$. Assuming that the shock travels at a uniform velocity $S_I k$, $S_I = M_S \sqrt{(\gamma_1 p_0) / \rho_1}$ is determined using the Rankine–Hugoniot conditions, and then the accelerating time and period are, respectively, approximated as

$$t_I = \frac{L/2 + Z_0 - a_0}{S_I} = \frac{L + 2(Z_0 - a_0)}{2M_S} \sqrt{\frac{\rho_1}{\gamma_1 p_0}} \quad (3.1)$$

and

$$\delta t_I = \frac{2a_0}{S_I} = \frac{2a_0}{M_S} \sqrt{\frac{\rho_1}{\gamma_1 p_0}}. \quad (3.2)$$

Before the incident shock accelerates the interface at $t < t_I$ in figure 3(a), the flow field is divided into a post-shock active region S with a finite velocity driven by the incident shock and two preshock quiescent regions 1 and 2. While the incident shock accelerates the interface at $t_I \leq t \leq t_I + \delta t_I$ in figure 3(b), the reflected shock is generated due to $\rho_2 > \rho_1$, and the incident shock across the interface becomes a transmitted shock. Due to the compression, the post-shock interface amplitude

$$a_0^+ \approx a_0 - \frac{1}{2} U_0^+ \delta t_I = \left(1 - \frac{U_0^+}{M_S} \sqrt{\frac{\rho_1}{\gamma_1 p_0}} \right) a_0 \quad (3.3)$$

is slightly reduced (see Richtmyer 1960), and the interface in (2.11) becomes

$$\varphi_I^+(x) = \frac{z}{a_0^+} - \cos(kx) \cos(ky) = 0. \quad (3.4)$$

Under the interfacial perturbation, both the reflected and transmitted shocks are distorted, followed by transverse waves (see Brouillette 2002), represented by dashed curves in figure 3(b,c). The transverse waves can further generate more complex waves, e.g. sound waves, and lead to pressure perturbations. In this stage, the flow field is divided into preshock regions 1 and 2 and post-shock regions S , 1^+ and 2^+ . The PBV is generated by the shock–interface interaction, which will be discussed in detail in § 3.2. After the transmitted shock leaves the interface at $t > t_I + \delta t_I$ in figure 3(c), preshock region 1 disappears. When the transmitted and reflected shocks with transverse waves are remote from the interface, only post-shock regions 1^+ and 2^+ remain in Ω .

A	A^+	T_1^+ (K)	T_2^+ (K)	p_0^+ (kPa)	a_0^+ (m)
0.30	0.32	313.9	299.5	128.8	3.4×10^{-3}
0.67	0.68	318.5	301.0	135.6	3.6×10^{-3}
0.80	0.81	320.9	301.7	139.1	3.7×10^{-3}

Table 2. Post-shock integral component of the quantities and post-shock Atwood number in the three DNS cases at various A .

To obtain the physical quantity \mathcal{P} for ρ , \mathbf{u} , p or T in post-shock regions 1^+ and 2^+ , we decompose

$$\mathcal{P}(\mathbf{x}, t) = \mathcal{P}^+(z, t) + \mathcal{P}'(\mathbf{x}, t) \tag{3.5}$$

into a post-shock integral component $\mathcal{P}^+(z, t)$ and a perturbed one $\mathcal{P}'(\mathbf{x}, t)$. Here $\mathcal{P}^+(z, t)$ is estimated by solving a one-dimensional Riemann problem along the z -direction (see Yang *et al.* 1994). The results indicate that post-shock regions 1^+ and 2^+ have different ρ_1^+ and ρ_2^+ , and T_1^+ and T_2^+ , whereas have the same $U_0^+ = U_0^+ \mathbf{k}$ and p_0^+ . The post-shock integral component of the quantities and the post-shock Atwood number

$$A^+ = \frac{\rho_2^+ - \rho_1^+}{\rho_1^+ + \rho_2^+} \tag{3.6}$$

in regions 1^+ and 2^+ in the three DNS cases at various A are calculated and listed in table 2.

When the incident shock accelerates the interface at $t_I \leq t \leq t_I + \delta t_I$, we approximate

$$\rho^+(\mathbf{x}, t) = \Delta\rho^+ \mathcal{H}(\varphi_I^+) + \rho_1^+, \tag{3.7}$$

$$p^+(\mathbf{x}, t) = -\Delta p^+ \mathcal{H}(\xi) + p_0^+ \tag{3.8}$$

and

$$T^+(\mathbf{x}, t) = \Delta T^+ \mathcal{H}(\varphi_I^+) + T_1^+, \tag{3.9}$$

where the post-shock density and temperature differences across the interface $\varphi_I = 0$ are $\Delta\rho^+ = \rho_2^+ - \rho_1^+$ and $\Delta T^+ = T_2^+ - T_1^+$, respectively, and the pressure difference across the distorted shock located at $\xi(\mathbf{x}, t)=0$ is $\Delta p^+ = p_0^+ - p_0$.

Moreover, $\mathcal{P}'(\mathbf{x}, t)$ in (3.5) contains effects of the PBV-induced velocity near the interface and of the pressure perturbations from the distorted transmitted/reflected shocks with transverse waves, which will be discussed in § 4.1 in detail.

3.2. Determination of the PBV

Taking the curl of (2.2) yields the vorticity equation

$$\frac{D\boldsymbol{\omega}}{Dt} = \boldsymbol{\omega} \cdot \nabla \mathbf{u} - \boldsymbol{\omega}(\nabla \cdot \mathbf{u}) + \frac{1}{\rho^2} (\nabla \rho \times \nabla p) + \bar{\nu} \nabla^2 \boldsymbol{\omega}, \tag{3.10}$$

where $D/Dt = \partial/\partial t + \mathbf{u} \cdot \nabla$ is the material derivative, $\boldsymbol{\omega} = \nabla \times \mathbf{u} = \omega_x \mathbf{i} + \omega_y \mathbf{j} + \omega_z \mathbf{k}$ the vorticity and $\bar{\nu} = \bar{\mu}/\rho$ the kinematic mixture viscosity.

We assume that $\boldsymbol{\omega}$ is generated post-shock (see Rasmus *et al.* 2018) at the intersection of the shock and interface, and neglect viscous effects (see Samtaney & Zabusky 1994).

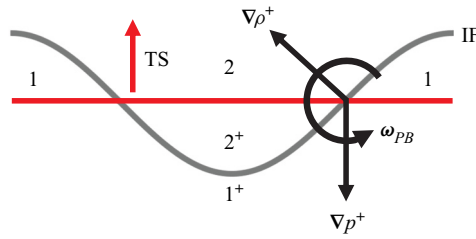


Figure 4. Schematic diagram of the production of PBV by the misalignment of the pressure gradient across the planar TS with the density gradient across the IF during their interaction.

Thus only the baroclinic term $(\nabla\rho \times \nabla p)/\rho^2$ remains on the right-hand side of (3.10). It is noted that the vorticity generation may be very complex from pressure perturbations of distorted shocks and transverse waves (e.g. Samtaney & Zabusky 1994; Samtaney, Ray & Zabusky 1998). As sketched in figure 4, we define that the PBV is generated at the interaction between the interface and the transmitted shock at $\xi(x, t) = [z - c(t)]/a_0^+ = 0$. In other words, we assume that the transmitted shock stays planar by removing the effects of pressure perturbations from distorted waves. Then we calculate the PBV

$$\omega_{PB}(x) = \int_{t_I}^{t_I+\delta t_I} \frac{D\omega}{Dt} dt = \int_{t_I}^{t_I+\delta t_I} \frac{1}{(\rho^+)^2} (\nabla\rho^+ \times \nabla p^+) dt \quad (3.11)$$

by integrating (3.10) between $t_I \leq t \leq t_I + \delta t_I$ in the Lagrangian view. Starting from (3.7) and (3.8), after some algebra (detailed in appendix A), we derive

$$\omega_{PB} = \frac{4A^+k\Delta p^+}{\bar{\rho}^+ \left(M_S \sqrt{\frac{\gamma_1 p_0}{\rho_1}} - U_0^+ \right)} \delta(\varphi_I^+) [K_y(x, y)\mathbf{i} + K_x(x, y)\mathbf{j}] \quad (3.12)$$

with

$$K_x(x, y) = \cos(kx) \sin(ky) \text{ and } K_y(x, y) = -\sin(kx) \cos(ky). \quad (3.13)$$

Hence, the PBV distribution is symmetric with respect to the interface and the plane $z = 0$.

Without loss of generality, we obtain the initial circulation

$$\Gamma_0 = \iint_{\mathbb{A}} \omega_{PB,x}(x = 0, y, z) dy dz = \frac{(4 + 2\pi)A^+ a_0 \Delta p^+}{M_S \bar{\rho}^+} \sqrt{\frac{\rho_1}{\gamma_1 p_0}} \quad (3.14)$$

through the right half of the symmetric slice

$$\mathbb{A} = \left\{ (y, z) \mid x = 0, \frac{L}{2} \leq y \leq L, -L \leq z \leq L \right\} \quad (3.15)$$

with $\omega_{PB} = \omega_{PB,x}\mathbf{i}$ and $\omega_{PB,x} > 0$ in \mathbb{A} . The initial circulations in the present DNS cases are calculated using (3.14) as $\Gamma_0 = 0.474, 0.706$ and $0.617 \text{ m}^2 \text{ s}^{-1}$ at $A = 0.30, 0.67$ and 0.80 , respectively.

We remark that Γ_0 in (3.14) is derived from the PBV in (3.12) rather than approximated by \dot{a}_0 in previous vortex models (e.g. Jacobs & Sheeley 1996; Likhachev & Jacobs 2005; Morgan *et al.* 2012). In addition, a more sophisticated estimation of Γ_0 was developed in Samtaney & Zabusky (1994) and Samtaney *et al.* (1998) by considering the effects of pressure perturbations such as the three-wave node.

3.3. VSF in the RMI

We use the VSF (see Yang & Pullin 2010) to visualize the evolution of vortical structures in the RMI. The VSF $\phi_v(\mathbf{x}, t)$ is a smooth scalar satisfying the constraint $\boldsymbol{\omega} \cdot \nabla \phi_v = 0$ so that $\boldsymbol{\omega}$ is tangent at every point (except for vorticity nulls) on an isosurface of ϕ_v , i.e. each VSF isosurface is a VS consisting of vortex lines. The VSF has been applied to transitional wall flows (Zhao, Yang & Chen 2016; Zhao *et al.* 2018), fully developed turbulence (Xiong & Yang 2019*b*), combustion (Zhou *et al.* 2019) and magnetohydrodynamics (Hao, Xiong & Yang 2019) to characterize vortex dynamics in the Lagrangian view.

Given the PBV in (3.12), the VSF at $t = t_I + \delta t_I$ is constructed as

$$\phi_{v0}(\mathbf{x}) = \frac{z}{a_0^+} - \exp\left(-[\varphi_I^+(\mathbf{x})]^{2m}\right) \cos(kx) \cos(ky) \tag{3.16}$$

with a weighting index m . Appendix B proves that $\phi_{v0}(\mathbf{x}) = 0$ is equivalent to $\varphi_I^+(\mathbf{x}) = 0$, so the isosurface of $\phi_{v0}(\mathbf{x}) = 0$ coincides with the interface $\varphi_I^+(\mathbf{x}) = 0$ at $t = t_I + \delta t_I$. We set a large $m = 10$ so that $\exp\{-[\varphi_I^+(\mathbf{x})]^{2m}\}$ decays rapidly for $\varphi_I^+ \neq 0$. The resultant approximation $\phi_{v0}(\mathbf{x}) \approx z/a_0^+$ implies that

$$\phi_{v0}(x, y, -z) \approx -\phi_{v0}(x, y, z) \tag{3.17}$$

is antisymmetric in the z -direction.

For this single-mode RMI with $\omega_z \approx 0$, we further demonstrate in appendix B that the VSF is simply governed by the Lagrangian transport equation

$$\frac{\partial \phi_v}{\partial t} + \mathbf{u} \cdot \nabla \phi_v = 0 \tag{3.18}$$

with the initial condition $\phi_v(\mathbf{x}, t = 0) = \phi_{v0}(\mathbf{x})$, i.e. the VS $\phi_v(\mathbf{x}, t) = 0$ coincides with the material interface in the entire evolution. The periodic boundary condition is applied for ϕ_v in the x - and y -directions, and an ‘opposite periodic’ boundary condition

$$\phi_{v0}(x, y, z = L, t) = -\phi_{v0}(x, y, z = -L, t) \tag{3.19}$$

is used in the z -direction owing to (3.17). The convection term of (3.18) is approximated by the fifth-order weighted essentially non-oscillatory scheme (Jiang & Shu 1996) and the integration in t is also marched by the third-order total-variation-diminishing Runge–Kutta scheme.

In the numerical implementation, (3.18) is solved along with the DNS. The temporal evolution of the VSF isosurface of $\phi_v = 0$ in this RMI at $A = 0.67$ is shown in figure 5. The surfaces are colour-coded by $0 \leq |\boldsymbol{\omega}|/|\boldsymbol{\omega}|_{max} \leq 0.8$, where $|\boldsymbol{\omega}|_{max}$ denotes the maximum of $|\boldsymbol{\omega}|$ in Ω . The moving direction of the surface can be inferred from the vortex lines on the surfaces with the Biot–Savart law. The PBV is deposited on the initial VS at $k\hat{a}_0(t_I + \delta t_I) = 0.013$ shortly after the shock accelerating the interface in figure 5(a), and then evolves through a short linear stage at $k\hat{a}_0 t = 1.0$ in figure 5(b) into asymmetric structures, i.e. spikes (upper part) and bubbles (lower part), in a nonlinear stage at $k\hat{a}_0 t = 3.0$ in figure 5(c). Finally the spikes and bubbles roll up into vortex rings at $k\hat{a}_0 t = 10$ in figure 5(d).

The VSF isoline of $\phi_v = 0$ and contours of ω_x for various A at a late time $k\hat{a}_0 t = 10$ are compared on the slice at $x = 0$ in figure 6. We observe that the separation between spikes and bubbles grows with A . In general, if the PBV with the same Γ_0 is added at the initial time, the roll-up of the interface is stronger for smaller A (e.g. Zabusky *et al.* 2003; Sohn 2004). On the other hand, Γ_0 calculated by (3.14) in the three DNS cases has

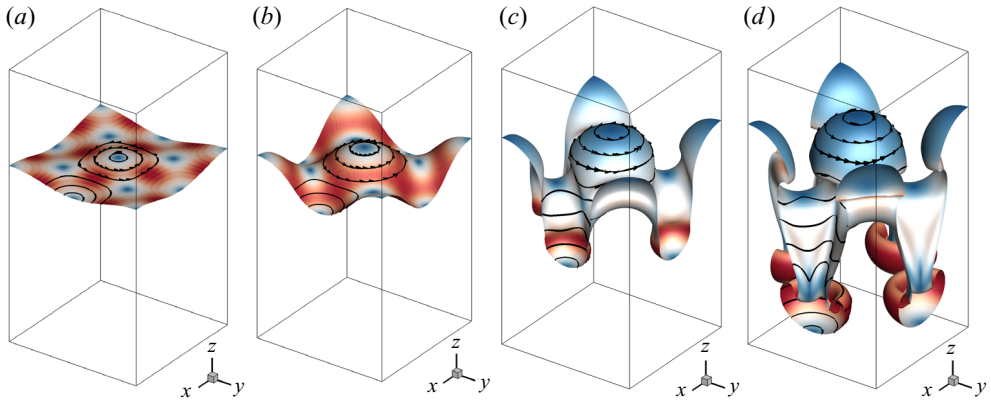


Figure 5. Temporal evolution of the VSF isosurface of $\phi_v = 0$ at (a) $k\hat{a}_0(t_I + \delta t_I) = 0.013$, (b) $k\hat{a}_0 t = 1.0$, (c) $k\hat{a}_0 t = 3.0$ and (d) $k\hat{a}_0 t = 10$ at $A = 0.67$. Some vortex lines are integrated and plotted on the surfaces colour-coded by $0 \leq |\omega|/|\omega|_{max} \leq 0.8$ from blue through white to red.

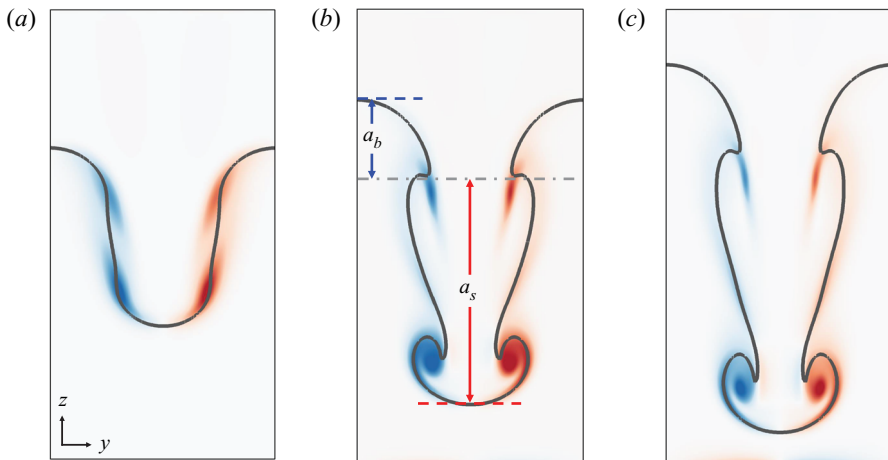


Figure 6. Comparison of the VSF isoline of $\phi_v = 0$ (solid line) and distribution of ω_x (colour-coded by $-0.8 \leq \omega_x/|\omega_x|_{max} \leq 0.8$ from blue through white to red) on the slice $x = 0$ at $k\hat{a}_0 t = 10$ with (a) $A = 0.30$, (b) $A = 0.67$ and (c) $A = 0.80$. The spike and bubble amplitudes calculated by (2.21) and (2.22) at $A = 0.67$ are marked in panel (b).

the maximum value at $A = 0.67$, and Γ_0 at $A = 0.67$ is nearly 1.5 times that at $A = 0.30$. As shown in figure 6(b), the vorticity at $A = 0.67$ is the most intensive and concentrated within spikes and bubbles, so the case at $A = 0.67$ with the notable vortex dynamics is used in the following analysis and modelling.

4. SBV

4.1. Double-density model of the RMI

As summarized in Nishihara *et al.* (2010), three types of perturbations, the density difference between the perturbed interface, the PBV and the pressure perturbation caused by distorted waves, can trigger the RMI. In order to distinguish the role of each factor, we

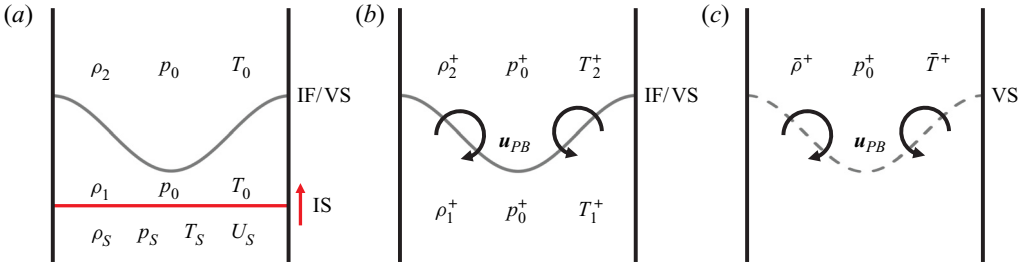


Figure 7. Schematic comparison of the initial conditions of the (a) RMI, (b) DDM and (c) SDM.

develop two simplified models, the double-density model (DDM) and the single-density model (SDM).

Initial conditions in the RMI, DDM and SDM are compared in figure 7. In the DDM with the density difference and PBV, the perturbed interface with amplitude a_0^+ separates the two fluids. The initial velocity u_{PB} is induced by the PBV in (3.12) for modelling the effect of the incident shock, and the pressure perturbation from distorted waves is excluded. In the SDM only with the PBV, the density is uniform without the interface and incident shock, and the PBV-induced velocity is imposed as in the DDM. Additionally, the VSF is constructed in both models, and the isosurface of $\phi_v = 0$ coincides with the interface in the RMI.

In the DDM, the initial flow field at $t = 0$ corresponds to that at $t = t_I + \delta t_I$ after the shock accelerating the interface in the RMI. The initial density, pressure and temperature are modelled by the post-shock integral quantities in regions 1^+ and 2^+ in figure 3(c) as

$$\rho_{DD}(\mathbf{x}, t = 0) = \Delta\rho^+ \mathcal{H}(\varphi_I^+) + \rho_1^+, \quad (4.1)$$

$$p_{DD}(\mathbf{x}, t = 0) = p_0^+, \quad (4.2)$$

$$T_{DD}(\mathbf{x}, t = 0) = \Delta T^+ \mathcal{H}(\varphi_I^+) + T_1^+. \quad (4.3)$$

The initial velocity

$$\mathbf{u}_{DD}(\mathbf{x}, t = 0) = \mathbf{u}_{PB}(\mathbf{x}) \quad (4.4)$$

is induced by the PBV in (3.12), where

$$\mathbf{u}_{PB}(\mathbf{x}) = \mathcal{F}^{-1} \left\{ \frac{i\mathbf{k}_F \times \mathcal{F}\{\boldsymbol{\omega}_{PB}\}}{|\mathbf{k}_F|^2} \right\} \quad (4.5)$$

is obtained by the Biot–Savart law (see Xiong & Yang 2019a) with the wavenumber \mathbf{k}_F in Fourier space and operators of the Fourier transform $\mathcal{F}\{\cdot\}$ and inverse Fourier transform $\mathcal{F}^{-1}\{\cdot\}$. Other fluid quantities μ , D , γ and κ are the same as those in the RMI.

In the SDM, the initial density

$$\rho_{SD}(\mathbf{x}, t = 0) = \bar{\rho}^+ = \frac{1}{2} (\rho_1^+ + \rho_2^+) \quad (4.6)$$

and temperature

$$T_{SD}(\mathbf{x}, t = 0) = \bar{T}^+ = \frac{1}{2} (T_1^+ + T_2^+) \quad (4.7)$$

are set to the averages of integral ones in post-shock regions 1^+ and 2^+ . The initial pressure and velocity are the same as (4.2) and (4.4) in the DDM, respectively. Then μ , D , γ and κ in the SDM are also set to be the averaged ones.

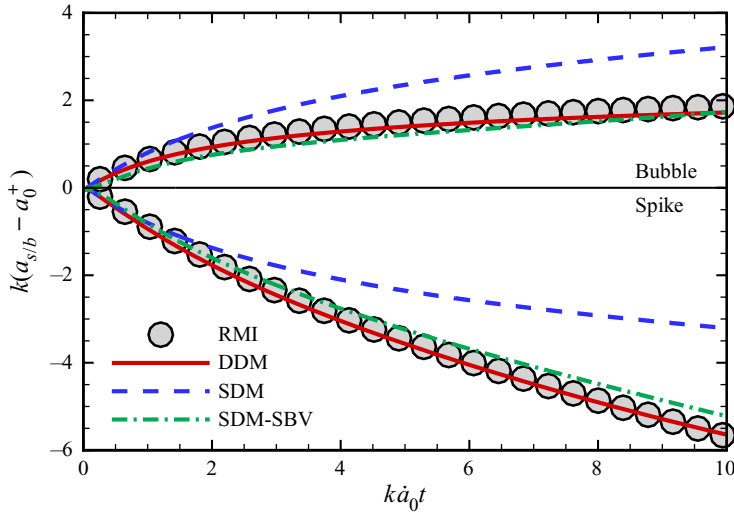


Figure 8. Temporal evolution of the scaled amplitudes of the spike and bubble in the RMI at $A = 0.67$ and corresponding DDM, SDM and SDM-SBV (discussed in § 4.4).

We examine the DDM and SDM corresponding to the RMI at $A = 0.67$. The simulations of the DDM and SDM are essentially the same as the DNS of the RMI except for using different initial conditions and removing the sponge layers. The evolution of the scaled spike and bubble amplitudes $k(a_{s/b} - a_0^+)$ are shown in figure 8, where the dimensionless time for the RMI in figure 8 has $k\dot{\alpha}_0(t_I + \delta t_I)$ subtracted. The amplitudes in the DDM are nearly identical to those in the RMI, and both DDM and RMI show the asymmetric growth of spikes and bubbles. By contrast, the structural evolution is symmetric in the SDM.

The VSF isosurface of $\phi_v = 0$ in the RMI, DDM and SDM are compared at a late time $k\dot{\alpha}_0 t = 10$ in figure 9. Note this VS is equivalent to the interface in the RMI and DDM, and there is no interface in the SDM. We observe spikes and bubbles in the RMI and DDM and symmetric structures in the SDM, consistent with the results in figure 8.

The nearly identical evolutions in the RMI and DDM demonstrate that the present single-mode RMI is mainly triggered by the density difference across the perturbed interface and PBV, whereas the pressure perturbation from distorted waves can be neglected. Therefore, the dynamical process of the VSF isosurface $\phi_{v0} = 0$ driven by the vorticity-induced velocity in the DDM can model the nonlinear growth of the interface in the RMI, and the VS will refer to the isosurface of $\phi_{v0} = 0$ in the rest of this paper.

4.2. Generation of the SBV

Next we use the DDM to clarify each role of the density difference and the PBV in the nonlinear evolution of the VS in the RMI. The symmetric slice at $x = 0$, containing the essential evolutionary geometry of VSs, is chosen to analyse vortex dynamics in the three-dimensional single-mode RMI. From the symmetries with $u_x = 0$, $\omega_y = \omega_z = 0$ and $\partial/\partial x = 0$, we have simplifications $\mathbf{x} = y\mathbf{j} + z\mathbf{k}$, $\nabla = (\partial/\partial y)\mathbf{j} + (\partial/\partial z)\mathbf{k}$, $\mathbf{u} = u_y\mathbf{j} + u_z\mathbf{k}$ and $\boldsymbol{\omega} = \omega_x\mathbf{i}$, and presume that the flow is nearly incompressible for low M_S without shocks (see Meiron & Meloon 1997; Kotelnikov, Ray & Zabusky 2000). In this way, the vorticity

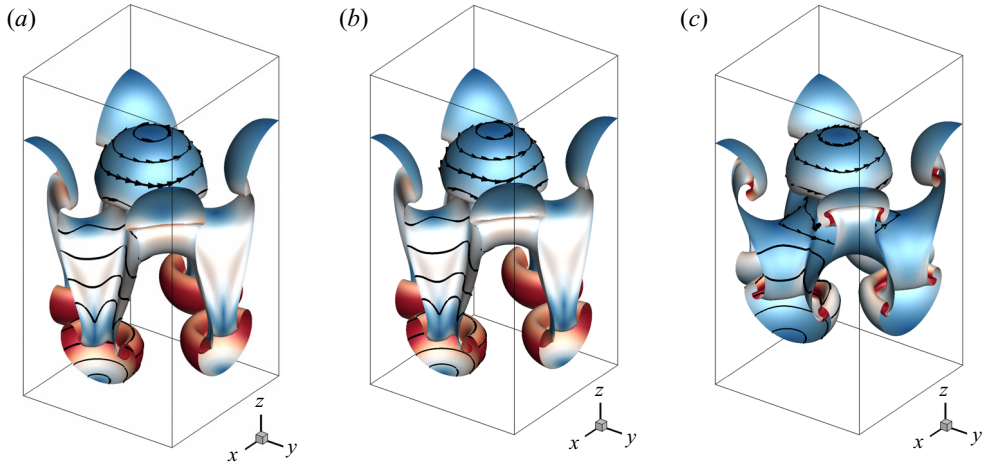


Figure 9. Comparison of the VSF isosurface of $\phi_v = 0$ of the (a) RMI, (b) DDM and (c) SDM for $A = 0.67$ at $k\hat{a}_0 t = 10$. Some vortex lines are integrated and plotted on the vortex surface colour-coded by $0 \leq |\omega|/|\omega|_{max} \leq 0.8$ from blue through white to red.

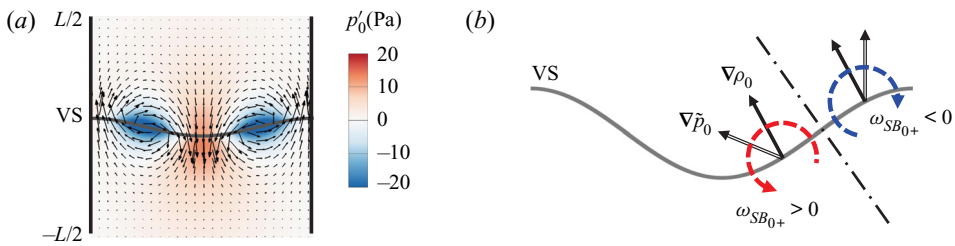


Figure 10. Generation mechanism of the SBV. (a) Distributions of the initial PBV-induced velocity (vectors) and the pressure perturbation (the contour colour-coded by $-20 \text{ Pa} \leq p'_0 \leq 20 \text{ Pa}$ from blue through white to red) on the slice of $x = 0$ within $-L/2 \leq z \leq L/2$. (b) Schematic diagram for the generation of the SBV at $t = 0^+$ owing to the misalignment of $\nabla\rho_0$ (solid arrows) across the VS with $\nabla\tilde{p}_0$ (open arrows) in the low-pressure region.

equation (3.10) on the plane $x = 0$ is simplified to

$$\frac{D\omega}{Dt} = \frac{1}{\rho^2} (\nabla\rho \times \nabla p) + \bar{v}\nabla^2\omega \quad (4.8)$$

with

$$\nabla\rho \times \nabla p = \frac{\partial\rho}{\partial y} \frac{\partial p}{\partial z} - \frac{\partial\rho}{\partial z} \frac{\partial p}{\partial y}. \quad (4.9)$$

Since the viscous term $\bar{v}\nabla^2\omega$ uniformly diffuses ω , the asymmetry of ω can be only contributed from the baroclinic term $(\nabla\rho \times \nabla p)/\rho^2$.

The initial density $\rho_0 = \rho_{DD}$ in (4.1) varies across the interface, so $\nabla\rho_0$ is normal to the VS pointing to the heavy fluid, marked by solid arrows in figure 10(b). Considering the right half-wave of the VS with the symmetry axis marked by the dash-dotted line in figure 10(b), $\nabla\rho_0$ is antisymmetric with respect to the symmetry axis.

Applying the decomposition (3.5) to the initial pressure \tilde{p}_0 in the DDM, we have

$$\tilde{p}_0(\mathbf{x}) = p_0^+ + p'_0(\mathbf{x}). \quad (4.10)$$

As the pressure perturbation from distorted waves has been excluded in the DDM, $p'_0(\mathbf{x})$ is only generated by the induced velocity of the PBV, and is governed by the variable-density pressure Poisson equation

$$\nabla^2 p'_0 = \frac{1}{\rho_0} (\nabla \rho_0 \cdot \nabla p'_0) - \rho_0 \nabla \mathbf{u}_{PB} : \nabla \mathbf{u}_{PB}, \quad (4.11)$$

which is obtained by taking the divergence of (2.2) and neglecting $\nabla \cdot \mathbf{u}$. By solving (4.11) using the iteration method with the initial condition $p'_0 = 0$, $p'_0(\mathbf{x})$ is obtained and plotted in figure 10(a), together with the PBV-induced velocity.

We find that the velocity induced by the PBV is continuous owing to the finite thickness of the interface approximated by (2.20). The distribution of \mathbf{u}_{PB} depicts a pair of counter-rotating vortices with the mirror symmetry with respect to the line $x = 0, y = L/2$. The vortices produce low pressure regions via (4.11), and $\nabla \tilde{p}_0$ is symmetric with respect to the symmetry axis of the right half of the VS, marked by open arrows in figure 10(b).

This misalignment of $\nabla \rho_0$ and $\nabla \tilde{p}_0$ produces another type of the baroclinic vorticity, referred to as the SBV. Being different from the PBV, the pressure gradient in the generation of the SBV is due to the low pressure region rather than the discontinuity of the incident shock.

4.3. Spikes and bubbles driven by the SBV

From the Lagrangian view, ω can be obtained by integrating the right-hand side of (4.8) and decomposed into

$$\omega(\mathbf{x}, t) = \omega_{SB}(\mathbf{x}, t) + \omega_v(\mathbf{x}, t) + \omega_0(\mathbf{x}) \quad (4.12)$$

with the SBV

$$\omega_{SB}(\mathbf{x}, t) = \int_0^t \frac{1}{\rho^2(\mathbf{x}, t')} [\nabla \rho(\mathbf{x}, t') \times \nabla p(\mathbf{x}, t')] dt', \quad (4.13)$$

the component produced by the viscous term

$$\omega_v(\mathbf{x}, t) = \int_0^t \bar{v}(\mathbf{x}, t') \nabla^2 \omega(\mathbf{x}, t') dt' \quad (4.14)$$

and the initial vorticity $\omega_0 = \omega_{PB,x}$.

At $t = 0^+$ shortly after the initial time in the DDM, the SBV is approximated by $\omega_{SB_{0+}} = (\nabla \rho_0 \times \nabla \tilde{p}_0) \Delta t / \rho_0^2$ as sketched by dashed curves with arrows in figure 10(b). We find that $\omega_{SB_{0+}}$ has opposite signs around the symmetry axis of the right half of the VS.

The synergistic effect of the PBV and SBV on the generation of spikes and bubbles is depicted on the right half of the VS in figure 11(a). Owing to the opposite signs of $\omega_{SB_{0+}}$, ω increases and decreases on the two sides of the symmetry axis marked by the dash-dotted line in figure 11(b), so the vorticity at $t = 0^+$ becomes asymmetric. Driven by the induced velocities of the PBV and SBV, the acceleration of the trough and deceleration of the crest of the VS leads to spikes and bubbles in the temporal evolution, respectively, as sketched in figure 11(b).

Therefore, the SBV is not only important in the late mixing stage in the RMI (see Peng *et al.* 2003; Zabusky *et al.* 2003), but also plays a key role in the asymmetric evolution

Mechanism and modelling of SBV in RMI

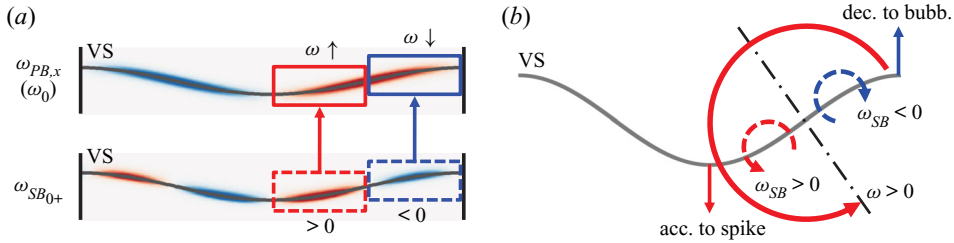


Figure 11. Generation mechanism of spikes and bubbles. (a) Contours of ω_{PB} and ω_{SB0+} at $t = 0^+$ on the slice of $x = 0$ near the VS. They are colour-coded by $-1.5 \times 10^5 \text{ s}^{-1} \leq \omega_{PB} \leq 1.5 \times 10^5 \text{ s}^{-1}$ and $-15 \text{ s}^{-1} \leq \omega_{SB0+} \leq 15 \text{ s}^{-1}$ from blue through white to red. (b) Schematic diagram for the generation of spikes and bubbles (bubb.) owing to acceleration (acc.) and deceleration (dec.) of the VS driven by the SBV.

of the VS at early times. To quantify the persistent effects of the SBV, we calculate the evolution of the circulation and its components

$$\Gamma(t) = \iint_{\mathbb{A}} \omega(\mathbf{x}, t) \, dy \, dz = \gamma_{SB}(t) + \gamma_v(t) + \Gamma_0 \quad (4.15)$$

by integrating (4.12) in region \mathbb{A} in (3.15), where the SBV component $\gamma_{SB}(t)$ and viscous component $\gamma_v(t)$ are the integrals of $\omega_{SB}(\mathbf{x}, t)$ and $\omega_v(\mathbf{x}, t)$ over \mathbb{A} , respectively, and the initial circulation in (3.14) is $\Gamma_0 = 0.706 \text{ m}^2 \text{ s}^{-1}$ at $A = 0.67$. We remark that (4.15) is an approximation, because the dilatation effect is neglected in (4.8).

Moreover, we further divide \mathbb{A} into the spike region \mathbb{A}_s and bubble region \mathbb{A}_b with $\mathbb{A} = \mathbb{A}_s \cup \mathbb{A}_b$ based on the evolving vortex surface (see appendix C), and decompose the circulation into

$$\Gamma(t) = \Gamma_s(t) + \Gamma_b(t) = \iint_{\mathbb{A}_s} \omega(\mathbf{x}, t) \, dy \, dz + \iint_{\mathbb{A}_b} \omega(\mathbf{x}, t) \, dy \, dz. \quad (4.16)$$

This decomposition also applies to the components in (4.15) as $\gamma_{SB}(t) = \gamma_{SB}^s(t) + \gamma_{SB}^b(t)$, $\gamma_v(t) = \gamma_v^s(t) + \gamma_v^b(t)$ and $\Gamma_0 = \Gamma_s(0) + \Gamma_b(0)$ with $\Gamma_s(0) = \Gamma_b(0) = \Gamma_0/2 = 0.353 \text{ m}^2 \text{ s}^{-1}$.

The difference in the evolutions of $\Gamma_s(t)$ and $\Gamma_b(t)$ contributes to the asymmetric growth of the VS via the vorticity-induced velocities (see figure 11). The temporal evolution of circulation variations $\Delta\Gamma_{s/b} = \Gamma_{s/b} - \Gamma_0/2$ and circulation components scaled by Γ_0 in spike and bubble regions in figure 12 shows that the SBV keeps influencing vortex motions. The positive γ_{SB}^s in spike regions increases ω and the negative γ_{SB}^b in bubble regions decreases ω . Moreover, $\gamma_{SB}^{s/b}$ are very close to $\Delta\Gamma_{s/b}$ in both regions, whereas $\gamma_v^{s/b}$ can be neglected. Therefore, the nonlinear growth of the interface in the RMI is persistently driven by the SBVs with opposite signs in spike and bubble regions. This SBV effect also provides a physical interpretation for the acceleration/deceleration caused by the perturbation parameter in the perturbation analysis of RMI (see Velikovich *et al.* 2014).

4.4. SDM with the time-varying SBV

The discussions in §§ 4.2 and 4.3 suggest that a major role of the density difference is to produce the SBV which dominates the nonlinear growth of the interface. To further support this important modelling ingredient, we simplify the DDM into the SDM with

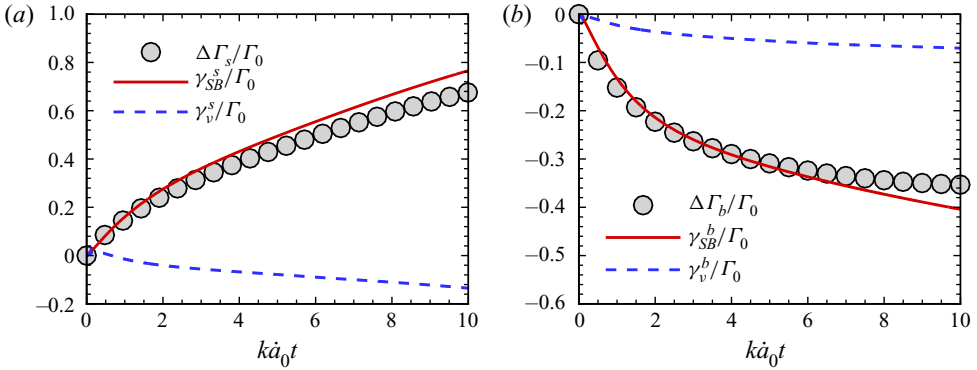


Figure 12. Temporal evolution of the scaled circulation variations, SBV and viscous components of the circulation in the (a) spike and (b) bubble regions.

the time-varying SBV (SDM–SBV). The initial conditions of the SDM–SBV are the same as those in the SDM, including the PBV and uniform density $\bar{\rho}^+$, pressure p_0^+ and temperature \bar{T}^+ , except that a source term is added to the momentum equation (2.2) as

$$\frac{\partial(\rho\mathbf{u})}{\partial t} + \nabla \cdot (\rho\mathbf{u}\mathbf{u} + p\mathbf{l} - \boldsymbol{\tau}) = \boldsymbol{\Xi}_{SB} \quad (4.17)$$

for the simulation of the SDM–SBV. Here, the source term is

$$\boldsymbol{\Xi}_{SB} = \frac{\partial(\rho\mathbf{u}_{SB})}{\partial t}, \quad (4.18)$$

where the SBV-induced velocity

$$\mathbf{u}_{SB}(\mathbf{x}) = \mathcal{F}^{-1} \left\{ \frac{i\mathbf{k}_F \times \mathcal{F}\{\boldsymbol{\omega}_{PB}\}}{|\mathbf{k}_F|^2} \right\} \quad (4.19)$$

is calculated from the DDM. The evolution of the scaled amplitudes $k(a_{s/b} - a_0^+)$ of the SDM–SBV generally agrees with those in the RMI and DDM in figure 8.

In summary, the nonlinear interfacial evolution of the present RMI can be modelled using the PBV and SBV in a uniform mixture without the density difference and shocks. The PBV first drives the interfacial instability, and then the SBV alters the vorticity distribution, leading to the nonlinear interfacial growth. The evolution of the modelling strategy with the increasing simplification level is illustrated in figure 13.

5. Modelling of spike and bubble growth rates

5.1. Vortex-ring model for the RMI

Inspired by the simplifications in the SDM–SBV, we model the interfacial evolution of spikes and bubbles in the RMI by two series of vortex rings moving in opposite directions in a uniform mixture without shocks, so the growth rates $\dot{a}_s(t)$ and $\dot{a}_b(t)$ are estimated by the velocities of corresponding vortex rings in the z -direction. This model in a periodic box is illustrated in figure 14(a). Considering the periodic boundary conditions, the model with infinite series of vortex rings in the top view is sketched in figure 14(b).

The spikes and bubbles are modelled by evolving vortex rings with different circulations. We introduce moving dual polar coordinates to characterize the motion of a vortex ring

Mechanism and modelling of SBV in RMI

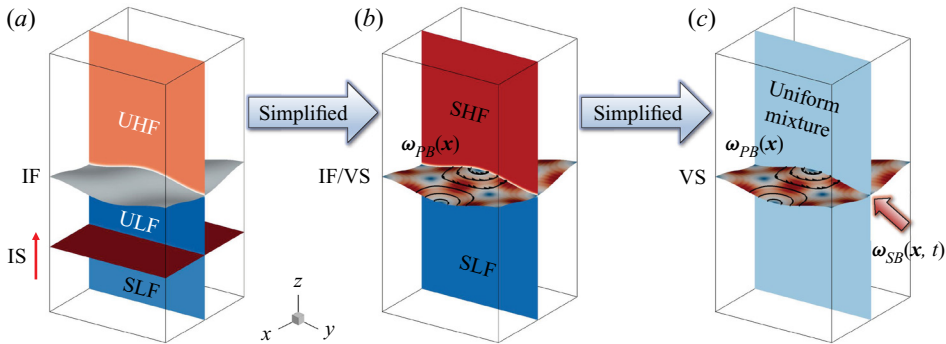


Figure 13. Schematic diagram of the simplification from (a) the RMI with the IS and IF separating two fluids, through panel (b) the DDM with the interface/VIS separating two fluids and the imposed PBV, to (c) the SDM-SBV with the uniform mixture, imposed the PBV and SBV. The symmetry plane $x = L/2$ is coloured by $\rho_1 \leq \rho \leq \rho_2$ from blue through white to red.

in figure 15. In this coordinate system moving with the vortex ring, the polar coordinates (R, θ) are built for the vortex ring with the origin at the ring centre, and (r, φ) are built on a cross-section of the ring with the origin at the central axis of the ring. Given the radius $R(t)$ of the vortex ring at a particular time, spatial coordinates (r, φ, θ) , with unit basis \mathbf{e}_r , \mathbf{e}_φ and \mathbf{e}_θ , are related to the Cartesian coordinates by

$$x = [R(t) + r \cos \varphi] \cos \theta, \quad y = [R(t) + r \cos \varphi] \sin \theta, \quad z = r \sin \theta. \quad (5.1a,b)$$

We assume that $\boldsymbol{\omega}(\mathbf{x}, t) = \omega_\theta(r, t)\mathbf{e}_\theta$ is uniform along the θ -direction in this model, then the circulation

$$\Gamma(t) = \int_0^{2\pi} d\varphi \int_0^\infty \omega_\theta(r, t) r dr \quad (5.2)$$

determines the velocity of the vortex ring. Since figure 12 shows that the circulations vary with time under the influence of the SBV and they are very different between spikes and bubbles, we divide the modelling of $\dot{a}_{s/b}(t)$ into two steps: (i) model the temporal evolution of $\Gamma_{s/b}(t)$ affected by the SBV; (ii) model $\dot{a}_{s/b}(t)$ based on the modelled $\Gamma_{s/b}(t)$ of vortex rings.

5.2. Modelling of circulations based on the SBV

The circulation of vortex rings is estimated by the integration (5.2) of $\omega_\theta(r, t)$, which models the SBV effect in the RMI and SDM-SBV. We propose several assumptions on the evolution of vortex rings as follows.

- (i) All the physical quantities are uniform along the θ -direction, i.e. $\partial/\partial\theta = 0$.
- (ii) The velocity only has the φ -component and is uniform in the φ -direction, i.e. $\mathbf{u} = u_\varphi(r, t)\mathbf{e}_\varphi$.
- (iii) The vorticity only has the θ -component and is uniform in the θ -direction, i.e. $\boldsymbol{\omega} = \omega_\theta(r, t)\mathbf{e}_\theta$.
- (iv) The flow is considered to be incompressible, because it has low M_S and no shock (see Meiron & Meloon 1997; Kotelnikov *et al.* 2000).

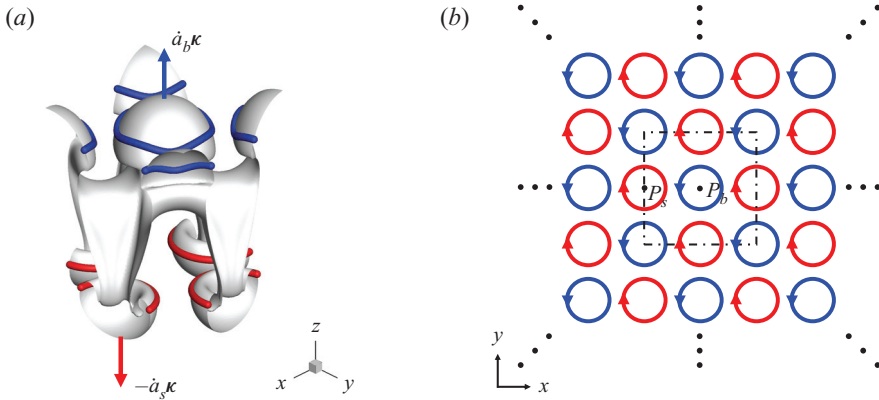


Figure 14. Schematic diagram of the vortex-ring model. (a) The spike and bubble modelled by vortex rings in a periodic box. The arrows denote the opposite moving directions of vortex rings with rates $\dot{a}_s(t)$ and $\dot{a}_b(t)$. (b) Configuration of periodic vortex rings in the entire domain in the top view. Red and blue rings are, respectively, vortex rings of spikes and bubbles. The arrow denotes vorticity direction and the dash-dotted box the boundary of a periodic box.

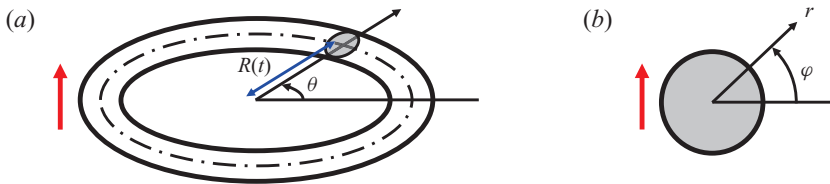


Figure 15. Schematic diagram of the moving dual polar coordinates, consisting of (a) polar coordinates for the vortex ring and (b) polar coordinates on a cross-section of the ring. The red arrow denotes the moving direction of the vortex ring at the rate $\dot{a}_s(t)$ or $\dot{a}_b(t)$.

Thus the vorticity equation (3.10) is simplified to

$$\frac{\partial \omega_\theta}{\partial t} = \mathcal{B}(\rho, p) + \mathcal{V}(\omega_\theta) \quad (5.3)$$

with the baroclinic term

$$\mathcal{B}(\rho, p) = \frac{1}{\rho^2 r} \frac{\partial \rho}{\partial \varphi} \frac{\partial p}{\partial r} \quad (5.4)$$

and the viscous term

$$\mathcal{V}(\omega_\theta) = \bar{\nu} \left(\frac{\partial^2 \omega_\theta}{\partial r^2} + \frac{1}{r} \frac{\partial \omega_\theta}{\partial r} \right). \quad (5.5)$$

Next, we re-express \mathcal{B} and \mathcal{V} in algebraic forms with known quantities.

In the SDM with vanishing $\mathcal{B}(\rho, p)$, the exact solution of (5.3) (see Tung & Ting 1967; Saffman 1970) is

$$\omega_\theta(r, t) = \frac{\Gamma_0}{4\pi \bar{\nu} t} \exp\left(-\frac{r^2}{4\bar{\nu} t}\right) \quad \text{and} \quad u_\varphi(r, t) = \frac{\Gamma_0}{2\pi r} \left(1 - \exp\left(-\frac{r^2}{4\bar{\nu} t}\right)\right), \quad (5.6a,b)$$

which implies that $\Gamma(t) = \Gamma_0$ is constant.

In the SDM–SBV and RMI, the influence of the SBV is introduced by finite $\mathcal{B}(\rho, p)$ in (5.3), leading to the time-varying $\Gamma(t)$. From (5.6a,b) and figure 6, we assume that

$$\omega_\theta(r, t) = \frac{\Gamma(t)}{4\pi\bar{\nu}t} \exp\left(-\frac{r^2}{4\bar{\nu}t}\right) \quad (5.7)$$

and

$$u_\varphi(r, t) = \frac{\Gamma(t)}{2\pi r} \left(1 - \exp\left(-\frac{r^2}{4\bar{\nu}t}\right)\right) \quad (5.8)$$

have Gaussian distributions along r . From (5.8), the radius of the vortex core

$$r_C(t) = 2\sqrt{\bar{\nu}t} \quad (5.9)$$

is defined by the distance from the ring centre to the location where u_φ peaks (see Saffman 1970).

To estimate $\mathcal{B}(\rho, p)$ in (5.3), we re-express the momentum equation (2.2) as

$$-\frac{u_\varphi^2}{r} = -\frac{1}{\rho} \frac{\partial p}{\partial r} \quad (5.10)$$

in cylindrical coordinates with the above assumptions, and then obtain the radial pressure gradient

$$\frac{\partial p}{\partial r} = \frac{\rho\Gamma^2(t)}{4\pi^2 r^3} \left(1 - \exp\left(-\frac{r^2}{4\bar{\nu}t}\right)\right)^2. \quad (5.11)$$

Subsequently, the azimuthal density gradient in $\mathcal{B}(\rho, p)$ in (5.4) is produced by the mass transfer owing to the roll-up of the interface between two fluids with ρ_1^+ and ρ_2^+ . Here, $\partial\rho/\partial\varphi$ is positive in the spike region where the heavy fluid is rolled into the light one. On the contrary, it is negative in the bubble region. Thus it is modelled by

$$\frac{\partial\rho}{\partial\varphi} = \pm \frac{\Delta\rho^+}{\Delta\varphi} \quad (5.12)$$

where the upper/lower sign applies to spikes/bubbles, and the variation of the azimuthal angle is calculated by the temporal integral of the angular velocity as

$$\Delta\varphi = \int_0^t \frac{u_\varphi(r, t')}{r} dt'. \quad (5.13)$$

To simplify (5.13) by removing the dependence on r , we approximate (5.8) by $u_\varphi(r, t) = u_\varphi(r_C, t)/2$, roughly the average of u_φ within the vortex ring. Then we derive

$$\Delta\varphi = \frac{(1 - e^{-1})\dot{a}_0}{16\pi\bar{\nu}k} \mathcal{G}(\Gamma, t) \quad \text{with } \mathcal{G}(\Gamma, t) = \int_0^t \frac{k\Gamma(t')}{\dot{a}_0 t'} dt', \quad (5.14)$$

where k and \dot{a}_0 are introduced to make \mathcal{G} dimensionless. Then (5.12) is approximated by

$$\frac{\partial\rho}{\partial\varphi} = \frac{\pm 16\pi\bar{\nu}k\Delta\rho^+}{(1 - e^{-1})\dot{a}_0\mathcal{G}(\Gamma, t)}. \quad (5.15)$$

Based on the SDM–SBV, we assume the uniform density $\rho = \bar{\rho}^+$ and the uniform averaged mixture kinematic viscosity

$$\bar{\nu} = \frac{\bar{\mu}}{\bar{\rho}^+} = \frac{\mu_1\sqrt{M_2} + \mu_2\sqrt{M_1}}{\bar{\rho}^+(\sqrt{M_1} + \sqrt{M_2})}, \quad (5.16)$$

where $\bar{\mu}$ is calculated from Reid *et al.* (1987) and μ_1 and μ_2 are, respectively, determined at T_1^+ and T_2^+ . In the three DNS cases, we obtain $\bar{v} = 5.61 \times 10^{-6}$, 3.74×10^{-6} and $2.31 \times 10^{-6} \text{ m}^2 \text{ s}^{-1}$ at $A = 0.30$, 0.67 and 0.80 , respectively. Substituting (5.11) and (5.15) into (5.4) and using $A^+ = \Delta\rho^+/(2\bar{\rho}^+)$ from (3.6) yields

$$\mathcal{B} = \frac{\pm 8A^+ \bar{v} k \Gamma^2(t)}{(1 - e^{-1}) \pi \dot{a}_0 r^4 \mathcal{G}(\Gamma, t)} \left(1 - \exp\left(\frac{r^2}{4\bar{v}t}\right) \right)^2. \tag{5.17}$$

Substituting (5.7) into (5.5) yields

$$\mathcal{V} = \frac{\Gamma(t)}{4\pi \bar{v} t^2} \left(\frac{r^2}{4\bar{v}t} - 1 \right) \exp\left(-\frac{r^2}{4\bar{v}t}\right). \tag{5.18}$$

Substituting (5.17) and (5.18) into (5.3) yields

$$\begin{aligned} \frac{\partial \omega_\theta}{\partial t} &= \frac{\pm 8A^+ \bar{v} k \Gamma^2(t)}{(1 - e^{-1}) \pi \dot{a}_0 r^4 \mathcal{G}(\Gamma, t)} \left(1 - \exp\left(-\frac{r^2}{4\bar{v}t}\right) \right)^2 \\ &+ \frac{\Gamma(t)}{4\pi \bar{v} t^2} \left(\frac{r^2}{4\bar{v}t} - 1 \right) \exp\left(-\frac{r^2}{4\bar{v}t}\right). \end{aligned} \tag{5.19}$$

Taking the time derivative of (5.7) yields

$$\frac{\partial \omega_\theta}{\partial t} = \frac{1}{4\pi \bar{v} t} \frac{d\Gamma}{dt} + \frac{\Gamma(t)}{4\pi \bar{v} t^2} \left(\frac{r^2}{4\bar{v}t} - 1 \right) \exp\left(-\frac{r^2}{4\bar{v}t}\right). \tag{5.20}$$

By equating (5.19) and (5.20), we have

$$\frac{d\Gamma}{dt} = \pm \frac{32A^+ k \bar{v}^2 t \Gamma^2(t)}{(1 - e^{-1}) \dot{a}_0 r^4 \mathcal{G}(\Gamma, t)} \left(\exp\left(\frac{r^2}{4\bar{v}t}\right) + \exp\left(-\frac{r^2}{4\bar{v}t}\right) - 2 \right). \tag{5.21}$$

This equation is further simplified, in appendix D, by approximating the exponential functions and removing the dependence on r .

Finally, we obtain the model equation of circulations for spikes/bubbles

$$\frac{d\Gamma_{s/b}}{dt} = \frac{\pm 2A^+ k \Gamma_{s/b}^2(t)}{(1 - e^{-1}) \dot{a}_0 (t + t_\delta) \mathcal{G}(\Gamma_{s/b}, t + t_\delta)} \tag{5.22}$$

with the initial condition $\Gamma_s(0) = \Gamma_b(0) = \Gamma_0/2$. Here, the singularity at $t = 0$ in (5.21) is removed by introducing a small $t_\delta = \delta_0^2/(4\bar{v})$, which is obtained from (5.9) by assuming the initial $r_C(t_\delta) = \delta_0$. Equation (5.22) implies that the SBV dominates the evolution of circulations, consistent with the numerical results in figure 12. We solve (5.22) numerically using the fourth-order Runge–Kutta method, and approximate the numerical solution by

$$\Gamma_{s/b}(t) = \Gamma_0 \left[0.5 \pm C_\Gamma (k \dot{a}_0 t)^{((3\pm 1)/4)A^+} \right] \tag{5.23}$$

with constant $C_\Gamma = 0.15$. In figure 16, the model results in (5.23) and numerical solutions of (5.22) generally agree with DNS results of the RMI, so the explicit expression (5.23) is used in the further modelling. The discrepancies may come from the assumption of ω_θ in (5.7), e.g. the distribution of ω_θ at $A = 0.30$ or for all the bubbles in figure 6 deviates from the Gaussian one.

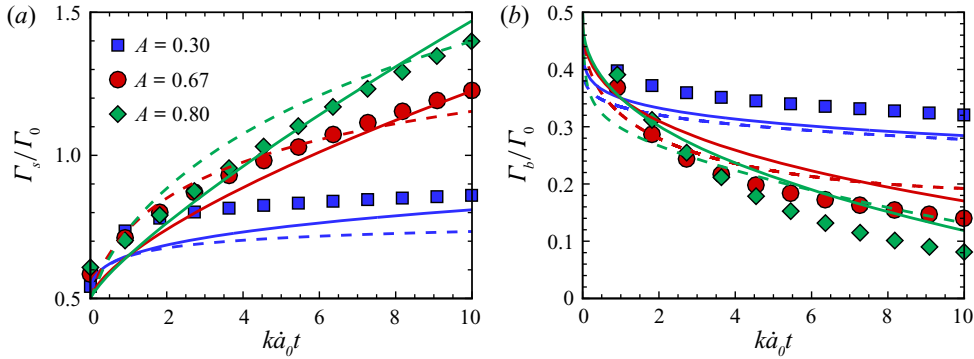


Figure 16. Comparisons of scaled circulations of the (a) spike and (b) bubble calculated from DNS (symbols), numerical solutions of (5.22) (dashed lines) and the model (5.23) (solid lines) at various A .

5.3. Modelling of growth rates using viscous vortex rings

The spike/bubble growth rate is modelled by the velocity of the vortex ring in the z -direction in this RMI. This velocity is the superposition of the self-induced velocity of the vortex ring and the induced velocities from infinite other vortex rings due to the periodicity in figure 14(b). However, the magnitude of the latter part decays as $O(r^{-2})$, so it can be absorbed into the leading terms as an amplification factor C_0 .

For example, the spike/bubble growth rate at P_s/P_b in figure 14(b) is approximated by the self-induced velocity of a vortex ring in viscous flows (see Saffman 1970; Fukumoto & Moffatt 2008)

$$\dot{a}_{s/b}(t) = \frac{C_0 \Gamma_{s/b}^E(t)}{4\pi^{4-n} R_b(t)} \left[\log \frac{4R_b(t)}{\sqrt{\bar{v}t}} - 3.672 \frac{\bar{v}t}{R_b^2(t)} - 0.558 \right], \quad (5.24)$$

with the number $n = 2, 3$ of dimensions, where the effective circulation

$$\Gamma_{s/b}^E(t) = \left[1 - \exp\left(-\frac{\alpha_v R_b^2(t)}{4\bar{v}t}\right) \right] \Gamma_{s/b}(t) \quad (5.25)$$

considers the vorticity cancellation at $r = 0$ (see Fukumoto & Kaplanski 2008) with a correction factor α_v in this RMI. It is noted that although the viscous effect is usually considered to be negligible in the interfacial growth (e.g. Carlès & Popinet 2002), it can be notable on the evolution of the vorticity distribution (e.g. Niederhaus & Jacobs 2003; Movahed & Johnsen 2013), especially near the vortex core via the vorticity cancellation, so it is still incorporated in (5.24) in our vortex-based modelling.

Then we assume that the spike/bubble radius $R_{s/b}(t) = R_0$ is invariant with time, where the initial radius

$$R_0 = \frac{\iiint_{\Omega} |\omega_{PB}| \sqrt{x^2 + y^2} dV}{\iiint_{\Omega} |\omega_{PB}| dV} = \frac{1}{k} \quad (5.26)$$

is calculated by the weighted-average distance. Since the maximal time scale in this RMI is $O(10^{-2})$ s, $3.672\bar{v}t/R_0^2 \ll \log(4R_0/\sqrt{\bar{v}t})$ is negligible in (5.24). Using a small drift time

Parameter	Physical meaning	Determination method
n	Number of dimensions	Given parameter
k	Wavenumber of the perturbed interface	Given parameter
A^+	Post-shock Atwood number	(3.6)
$\bar{\nu}$	Averaged mixture kinematic viscosity	(5.16)
\dot{a}_0	Initial growth rate	Initial data of DNS or experiment
Γ_0	Initial circulation	(3.14)

Table 3. Summary of the parameters in the model (5.28) of growth rates.

t_ϵ to remove the temporal singularity at $t = 0$, (5.24) becomes

$$\dot{a}_{s/b}(t) = \frac{C_0}{4\pi^{4-n}} k \Gamma_{s/b}(t) \left(1 - \exp\left(-\frac{\alpha_\nu}{4k^2\bar{\nu}t}\right) \right) \left[\log \frac{4}{k\sqrt{\bar{\nu}}(t+t_\epsilon)} - 0.558 \right]. \quad (5.27)$$

In the SDM with uniform density and $A = 0$, the circulations $\Gamma_s(t) = \Gamma_b(t) = \Gamma_0/2$ are constant and the growth rates $\dot{a}_s(t) = \dot{a}_b(t) = \dot{a}_{SD}(t)$ are symmetric. Then we obtain $C_0 = 1.3$ and $\alpha_\nu = 1.587 \times 10^{-4}$ by fitting $\dot{a}_{SD}(t)$ from the SDM result at $A = 0.67$. We remark that the two parameters obtained from this particular case appear to be universal, which is validated by further *a posteriori* model tests.

Substituting (5.23) and all the parameter values into (5.27), finally we obtain a predictive model for the spike/bubble growth rate as

$$\begin{aligned} \dot{a}_{s/b}(t) &= \frac{k\Gamma_0}{4\pi^{4-n}} \left[0.65 \pm 0.195 (k\dot{a}_0 t)^{(3\pm 1)/4} A^+ \right] \left[1 - \exp\left(-\frac{3.97 \times 10^{-5}}{k^2\bar{\nu}t}\right) \right] \\ &\times \left[\log \frac{4}{k\sqrt{\bar{\nu}}(t+t_\epsilon)} - 0.558 \right], \end{aligned} \quad (5.28)$$

where the positive/negative sign, respectively, applies to spikes/bubbles, and

$$t_\epsilon = \frac{16}{k^2\bar{\nu}} \exp\left(-12.31\pi^{4-n} \frac{\dot{a}_0}{k\Gamma_0} - 1.116\right) \quad (5.29)$$

is determined from $\dot{a}_s(0) = \dot{a}_b(0) = \dot{a}_0$. The physical meaning and determination method of the model parameters in (5.28) are summarized in table 3. From (5.28), we find that the nonlinear growth of the RMI mainly depends on A^+ , and is only slightly mitigated by the viscous effect (see Mikaelian 1993; Niederhaus & Jacobs 2003; Sohn 2009).

5.4. Model assessment

We assess the model in (5.28) using results from the present DNS and other four data sets in the literature, including DNS data of Latini, Schilling & Don (2007) and Long *et al.* (2009) and experimental data of Jacobs & Krivets (2005) and Liang *et al.* (2019) with key parameters summarized in table 4.

Figure 17 validates the model prediction using the present DNS result of scaled growth rates and amplitude variations at three A . In general, our model is able to predict the nonlinear growth of spikes and bubbles, and the predictions (solid lines) agree with the DNS results (symbols) at various A . The slight discrepancy of the model prediction is primarily due to the error from the circulation modelling in (5.22) and figure 16.

Parameter	Latini <i>et al.</i>	Long <i>et al.</i>	Jacobs & Krivets	Liang <i>et al.</i>
Type	DNS	DNS	Experiment	Experiment
n	2	3	2	2
a_0 (m)	2.00×10^{-3}	3.45×10^{-3}	2.90×10^{-3}	4.00×10^{-3}
λ (m)	0.0593	0.0889	0.0590	0.0600
M_S	1.210	1.220	1.292	1.200
p_0 (kPa)	95.60	101.3	101.3	101.3
T_0 (K)	296	293	293	293
A^+	0.61	0.69	0.71	0.57
\dot{a}_0 (m s ⁻¹)	7.020	12.08	10.55	12.05
\bar{v} (m ² s ⁻¹)	3.10×10^{-6}	2.81×10^{-6}	2.49×10^{-6}	5.62×10^{-6}
Γ_0 (m ² s ⁻¹)	0.517	1.05	1.03	0.983

Table 4. Parameters of DNS and experimental series in the literature.

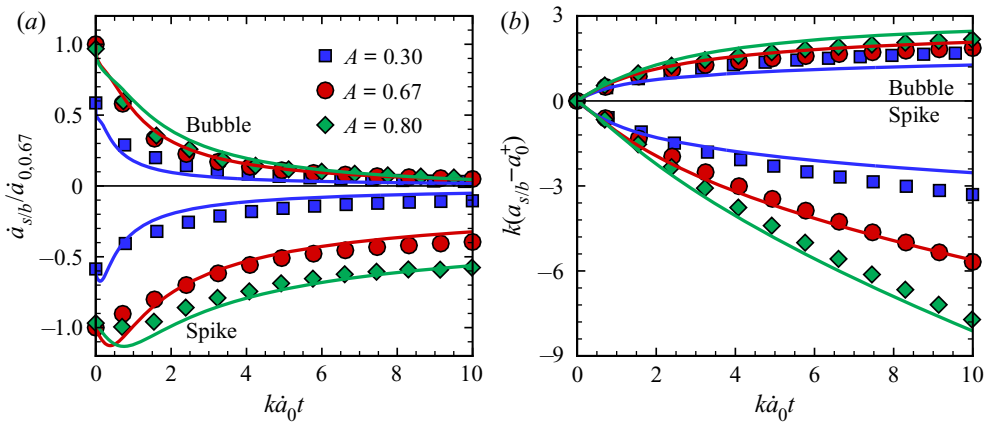


Figure 17. Comparisons of scaled (a) growth rates and (b) amplitudes of spikes and bubbles calculated from the DNS results of the RMI (symbols) with the present model (5.28) (solid lines) at various A . The growth rates are scaled by $\dot{a}_{0,0.67} \equiv \dot{a}_0 = 8.50 \text{ m s}^{-1}$ at $A = 0.67$ for distinguishing results at different A .

In figure 18, the comparison of the scaled amplitudes from model predictions of (5.28) (solid lines) and various DNS/experimental results (symbols) also shows overall good agreement.

In appendix E, the present model is compared with several existing models of spike and bubble growth rates for all the DNS/experimental series above. In general, the overall prediction from our vortex-based model is comparable or slightly better than the others. Therefore, we demonstrate that the model (5.28) can predict the nonlinear interfacial growth in the RMI at a range of parameters and with various initial conditions.

Compared with existing models, the features of the present one are summarized below.

- (i) Spike and bubble growth rates are modelled by the motion of vortex rings in viscous flows. The modelling is based on the dynamics of VSs, instead of the asymptotic analysis and empirical matching.

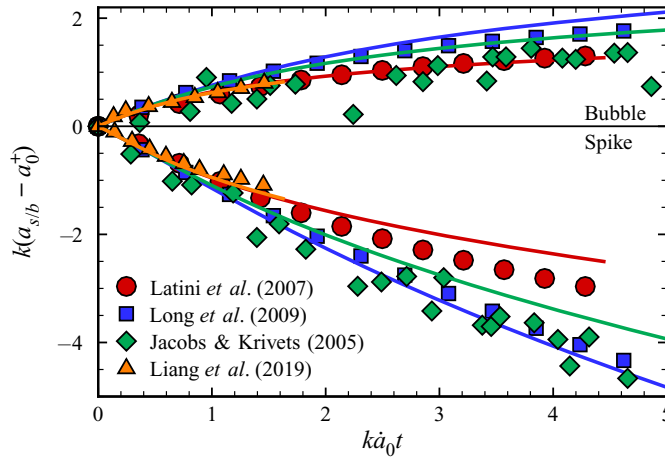


Figure 18. Comparisons of scaled spike and bubble amplitudes from the DNS and experimental results (symbols) with the present model (5.28) (solid lines). The line colour corresponds to the symbol colour for the comparison of the same series.

- (ii) The mechanism of the SBV is elucidated and used to model the increase or decrease of circulations, which leads to enhancement or suppression of the growth of spikes or bubbles, respectively.
- (iii) The present vortex-based model for two- and three-dimensional RMIs involves time-varying circulations. The initial circulation is derived from the explicit expression of the PBV rather than approximated by the initial growth rate.

On the other hand, the present model is based on the assumption of incompressible flows, so it is restricted to low M_S , e.g. $M_S < 1.3$ (see Peng *et al.* 2003) in table 4. Additionally, the pressure perturbation by distorted waves and the multimode initial perturbation in the complex RMI with reshocks and turbulent mixing (e.g. Hill, Pantano & Pullin 2006; Pantano *et al.* 2007) have not been considered.

6. Conclusions

In this study, we distinguish the effects of the PBV and SBV in the RMI accelerated by a weak incident shock, and demonstrate that the SBV plays an important role in the nonlinear growth of the interface. Then we develop a predictive model for spike and bubble growth rates based on the motion of viscous vortex rings with the effects of the SBV.

The present RMI arises from a planar shock at low $M_S = 1.1$ accelerating a single-mode light/heavy interface at $A = 0.30, 0.67$ and 0.80 in a shock tube. The PBV produced by the shock–interface interaction is derived in (3.12). The VSF is constructed and evolved with the DNS of the RMI. We find that the evolution of the interface with spikes and bubbles is driven by the dynamics of the VS.

In order to distinguish each role of the density difference across the perturbed interface, the PBV and the pressure perturbation required to trigger the nonlinear growth in the RMI, we develop two simplified models: the DDM excluding pressure perturbations and the SDM only with the PBV. The evolution of the VS with the generation of spikes and bubbles in the DDM is nearly identical to that in the corresponding RMI, whereas it remains symmetric in the SDM. Thus, this single-mode RMI is mainly triggered by the density difference and the PBV.

We elucidate the synergistic effect of the PBV and SBV on the generation of spikes and bubbles using the DDM. The SBV is generated by the misalignment between the density gradient across the interface and the pressure gradient within the low pressure region produced by the PBV-induced velocity. The SBV persistently accelerates or decelerates the interface via the velocity induced from the circulation of the VS, and leads to the nonlinear growth of the interface with spikes and bubbles. After the PBV deposited at the interface, the SBV leads to the nonlinear growth, so the RMI can be further simplified into the SDM–SBV with the uniform density, the imposed initial PBV and the temporally evolving SBV.

Inspired by this mechanism, we develop a vortex-based model for interfacial growth rates in the RMI. The spikes and bubbles are modelled by two series of vortex rings moving in opposite directions in viscous flows. Their growth rates are estimated by induced-velocities of corresponding vortex rings. The SBV effect is incorporated to model different time-varying circulations of spikes and bubbles, leading to asymmetric growth rates. We obtain a predictive model of spike and bubble growth rates in (5.28), which depends on initial conditions with a one-dimensional Riemann solution and \dot{a}_0 determined from the initial DNS or experimental data. Compared with existing models, the present one is based on dynamics of the VS rather than asymptotic analysis. The model is validated at a range of A and with various initial conditions by the present DNS and other four DNS/experimental data sets of the RMI in the literature.

The present model can be extended to more complex RMIs by considering the following effects: (i) compressibility for high M_S ; (ii) pressure perturbations caused by distorted waves, which can be important in RMI with reshocks (e.g. Hill *et al.* 2006; Thornber *et al.* 2012) and converging geometries (e.g. Lombardini & Pullin 2009); (iii) inclined (e.g. Hahn *et al.* 2011) or multimode perturbed initial interfaces triggering turbulent mixing (e.g. Zhou 2001; Thornber *et al.* 2011). Additionally, the vortex-based model can be extended to the Rayleigh–Taylor instability and the induced turbulent mixing (e.g. Zhou 2017a,b; Kokkinakis, Drikakis & Youngs 2019).

Acknowledgements. Numerical simulations were carried out on the TH-2A supercomputer in Guangzhou, China.

Funding. This work has been supported in part by the National Natural Science Foundation of China (grants nos. 11988102, 11925201, 91841302 and 91952108).

Declaration of interests. The authors report no conflict of interest.

Author ORCIDs.

-  Naifu Peng <https://orcid.org/0000-0003-0894-9045>;
-  Yue Yang <https://orcid.org/0000-0001-9969-7431>;
-  Jinxin Wu <https://orcid.org/0000-0003-4914-1886>;
-  Zuoli Xiao <https://orcid.org/0000-0001-6123-3404>.

Appendix A. Derivation of the PBV

Taking the gradient of (3.7) and (3.8) yields

$$\nabla \rho^+ = \rho_x^+ \mathbf{i} + \rho_y^+ \mathbf{j} + \rho_z^+ \mathbf{k} \tag{A1}$$

and

$$\nabla p^+ = -\frac{\Delta p^+}{a_0^+} \delta(\tilde{z}) \mathbf{k} \tag{A2}$$

with $\rho_x^+ = k\Delta\rho^+ \sin(kx) \cos(ky)\delta(\varphi_I^+)$, $\rho_y^+ = k\Delta\rho^+ \cos(kx) \sin(ky)\delta(\varphi_I^+)$, $\rho_z^+ = \Delta\rho^+ \delta(\varphi_I^+)/a_0^+$ and $\tilde{z} = [z - c(t)]/a_0^+$. Substituting (3.7), (A1) and (A2) into the baroclinic term in (3.10) yields

$$\frac{1}{(\rho^+)^2} (\nabla\rho^+ \times \nabla p^+) = \frac{k\Delta\rho^+ \Delta p^+}{a_0^+ [\Delta\rho^+ \mathcal{H}(\varphi_I^+) + \rho_1^+]^2} \delta(\varphi_I^+) \delta(\tilde{z}) [K_y(x, y)\mathbf{i} + K_x(x, y)\mathbf{j}], \tag{A3}$$

so the baroclinic term is non-vanishing only where the shock crosses the interface.

For the Heaviside function defined by

$$\mathcal{H}(\varphi_I^+) = \begin{cases} 0, & \varphi_I^+ < 0, \\ 1/2, & \varphi_I^+ = 0, \\ 1, & \varphi_I^+ > 0, \end{cases} \tag{A4}$$

(A3) is simplified to

$$\frac{1}{(\rho^+)^2} (\nabla\rho^+ \times \nabla p^+) = \frac{4k\Delta\rho^+ \Delta p^+}{a_0^+ (\rho_1^+ + \rho_2^+)^2} \delta(\varphi_I^+) \delta(\tilde{z}) [K_y(x, y)\mathbf{i} + K_x(x, y)\mathbf{j}]. \tag{A5}$$

Then substituting (A5) to (3.11) yields the PBV

$$\boldsymbol{\omega}_{PB} = \frac{4k\Delta\rho^+ \Delta p^+ \delta t_I}{a_0^+ (\rho_1^+ + \rho_2^+)^2} \delta(\varphi_I^+) [K_y(x, y)\mathbf{i} + K_x(x, y)\mathbf{j}]. \tag{A6}$$

Finally, substituting δt_I in (3.2) and a_0^+ in (3.3) to (A6) and replacing $\Delta\rho^+$ and $(\rho_1^+ + \rho_2^+)$ by A^+ and $\bar{\rho}^+$, we derive (3.12) for the PBV.

Appendix B. Evolution of the VSF in the RMI

The two-time method (Yang & Pullin 2011; Peng & Yang 2018) is used to calculate the VSF evolution. The temporal evolution at each time step is divided into prediction and correction substeps. In the prediction substep, the temporary VSF solution $\phi_v^*(\mathbf{x}, t)$ is evolved as a Lagrangian field as

$$\frac{\partial \phi_v^*(\mathbf{x}, t)}{\partial t} + \mathbf{u}(\mathbf{x}, t) \cdot \nabla \phi_v^*(\mathbf{x}, t) = 0, \quad t \geq 0 \tag{B1}$$

with the initial condition $\phi_v(\mathbf{x}, t = 0) = \phi_{v0}(\mathbf{x})$. Here, $\phi_v^*(\mathbf{x}, t)$ can slightly deviate from an accurate VSF owing to the breakdown of the Helmholtz vorticity theorem in non-ideal flows. In the correction substep, at a fixed physical time t , $\phi_v^*(\mathbf{x}, t)$ is transported along the frozen vorticity in pseudo time τ as

$$\frac{\partial \phi_v(\mathbf{x}, t; \tau)}{\partial \tau} + \boldsymbol{\omega}(\mathbf{x}, t) \cdot \nabla \phi_v(\mathbf{x}, t; \tau) = 0, \quad \tau \geq 0 \tag{B2}$$

with the pseudo initial condition $\phi_v(\mathbf{x}, t; \tau = 0) = \phi_v^*(\mathbf{x}, t)$, and then $\phi_v(\mathbf{x}, t)$ is updated by

$$\phi_v(\mathbf{x}, t) = \lim_{\tau \rightarrow \infty} \phi_v(\mathbf{x}, t; \tau) \tag{B3}$$

from (B2) when $\phi_v(\mathbf{x}, t; \tau)$ is converged.

We demonstrate that the isosurface of $\phi_v(\mathbf{x}, t) = 0$ can be tracked in time and it coincides with the interface. In the prediction substep, the solution

$$\phi_v^*(\mathbf{x}, t) = (-1)^{n_t(z-u_z t)} \phi_{v0}(\mathbf{x} - \mathbf{u}t) \tag{B4}$$

of (B1) is obtained from the Cauchy problem of the first-order quasi-linear hyperbolic equation (see Evans 1998) with the index

$$n_t(\alpha) = \begin{cases} \left\lfloor \frac{\alpha}{L} + \frac{1}{2} \right\rfloor + 1, & \alpha \geq L, \\ \left\lfloor \frac{\alpha}{L} + \frac{1}{2} \right\rfloor, & \alpha < L, \end{cases} \tag{B5}$$

to satisfy the ‘opposite periodic’ boundary condition (3.19) in the z -direction, where $\lfloor \cdot \rfloor$ is the floor function. Similarly, the solution of (B2) is

$$\phi_v(\mathbf{x}, t; \tau) = (-1)^{n_t(z-\omega_z \tau)} \phi_v^*(\mathbf{x} - \boldsymbol{\omega}\tau, t). \tag{B6}$$

In the present single-mode RMI perturbed in the x - and y -directions with $\omega_z \approx 0$, we obtain

$$\phi_v(\mathbf{x}, t) = \lim_{\tau \rightarrow \infty} (-1)^{n_t(\tilde{z})} \left\{ \frac{\tilde{z}}{a_0^+} - \exp\left(-[\varphi_I^+(\hat{\mathbf{x}})]^{2m}\right) \cos(k\hat{x}) \cos(k\hat{y}) \right\} \tag{B7}$$

by substituting (B6), (B4) and (3.16) to (B3), where $\hat{\mathbf{x}} = \hat{x}\mathbf{i} + \hat{y}\mathbf{j} + \tilde{z}\mathbf{k}$ denotes translated coordinates with $\hat{x} = x - u_x t - \omega_x \tau$, $\hat{y} = y - u_y t - \omega_y \tau$ and $\tilde{z} = z - u_z t$. Equation (B7) has $\phi_v(\mathbf{x}, t) = 0$ for $\varphi_I^+(\hat{\mathbf{x}}) = 0$ and

$$\phi_v(\mathbf{x}, t) \approx \frac{(-1)^{n_t(z-u_z t)}}{a_0^+} (z - u_z t) \tag{B8}$$

for $\varphi_I^+(\hat{\mathbf{x}}) \neq 0$, so the isosurface of $\phi_v(\mathbf{x}, t) = \psi$ is given by

$$z = \begin{cases} a_0^+ \lim_{\tau \rightarrow \infty} \cos[k(x - u_x t - \omega_x \tau)] \cos[k(y - u_y t - \omega_y \tau)] + u_z t, & \psi = 0, \\ (-1)^{n_t(z-u_z t)} a_0^+ \psi + u_z t, & \psi \neq 0. \end{cases} \tag{B9}$$

In (B9), the correction substep only influences the VSF isosurface of $\phi_v(\mathbf{x}, t) = 0$ consisting of vortex lines of $dx/\omega_x = dy/\omega_y$, but it does not change the surface geometry. Therefore, the isosurface of $\phi_v(\mathbf{x}, t) = 0$ describes the evolution of the same vortex surface and coincides with the interface, and the VSF evolution is only governed by (B1) in this single-mode RMI.

In general, there is a slight deviation of the numerical solution of ϕ_v from the exact one, and the VSF deviation is defined by (see Yang & Pullin 2010)

$$\lambda_\omega \equiv \frac{\boldsymbol{\omega} \cdot \nabla \phi_v}{|\boldsymbol{\omega}| |\nabla \phi_v|}. \tag{B10}$$

We find that the volume-averaged deviation $\langle |\lambda_\omega| \rangle$ in present DNS cases of the RMI at various A are negligible (less than 3%).

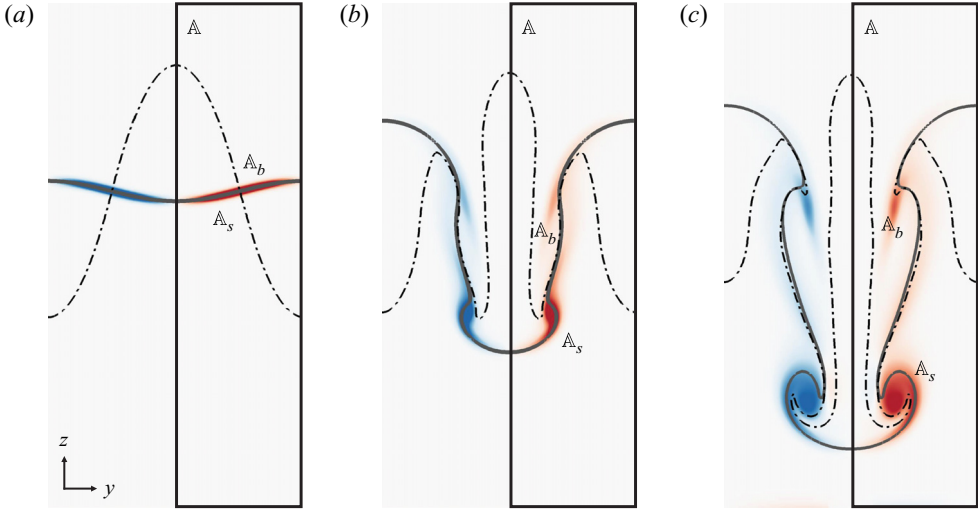


Figure 19. The boundary (dash-dotted line) separating integral regions of spikes and bubbles into $\mathbb{A} = \mathbb{A}_s \cup \mathbb{A}_b$ on $x = 0$ at (a) $k\hat{a}_0 t = 0$, (b) $k\hat{a}_0 t = 5$ and (c) $k\hat{a}_0 t = 10$, with the VS (solid line) and distribution of ω_x (colour-coded by $-0.8 \leq \omega_x/|\omega_x|_{max} \leq 0.8$ from blue through white to red).

Appendix C. Integral regions for circulations of spikes and bubbles

We determine the integral boundary separating the spike region \mathbb{A}_s and bubble region \mathbb{A}_b using the Lagrangian-based VSF. At the initial time, the distribution of ω_x has a symmetry on a half-plane at $x = 0$ in figure 19(a), so we use a piecewise function

$$\varphi_T(y, z) = z - \frac{L^2}{16\pi(a_0^+)^2} f_T(y) = 0 \tag{C1}$$

with

$$f_T(y) = \begin{cases} y^2 - Ly + \frac{3L^2}{16}, & \frac{L}{2} \leq x < \frac{3L}{4} \\ y^2 - 2Ly + \frac{15L^2}{16}, & \frac{3L}{4} \leq x \leq L \end{cases} \tag{C2}$$

to separate \mathbb{A}_s and \mathbb{A}_b , which is perpendicular to the VSF isosurface of $\phi_v = 0$ at $(y, z) = (3L/4, 0)$ marked by the dash-dotted line in figure 19(a), and is normalized by 1 m for consistent dimensions.

Then we construct a tracking function $\phi_T(y, z, t)$ with the initial condition $\phi_T(y, z, t = 0) = 1 - 2\mathcal{H}(\varphi_T)$. If ϕ_T is evolved by the VSF equation (3.18) on the plane $x = 0$, the isoline of $\phi_T = 0$ can be the region boundary as $\phi_T > 0$ for \mathbb{A}_s and $\phi_T < 0$ for \mathbb{A}_b , as shown in figure 19 together with the contour of ω_x and the VS. We observe that some parts of $\phi_T = 0$ are very close to the material surface at late times, but they do not divide the region with the concentrated vorticity magnitude. Therefore, $\phi_T = 0$ can still effectively separate spike and bubble regions with different blobs of concentrated ω_x in the evolution.

Appendix D. Simplification of the modelled circulation equation

In order to simplify (5.21), we approximate

$$\exp\left(\pm \frac{r^2}{4\bar{v}t}\right) \approx 1 \pm \frac{r^2}{4\bar{v}t} + \frac{r^4}{32\bar{v}^2t^2} \tag{D1}$$

using the Taylor expansion, so that the dependence of (5.21) on r is removed as

$$\frac{d\Gamma}{dt} = \frac{\pm A^+ k \Gamma^2(t)}{(1 - e^{-1}) \mathcal{G}(\Gamma, t)} \mathcal{Q}_T(t) \tag{D2}$$

with

$$\mathcal{Q}_T(t) = \frac{2}{k\dot{a}_0 t}. \tag{D3}$$

We remark that the requirement $r \ll r_C$ for the Taylor expansion in (D1) may not hold in this model, so we perform another derivation directly from (5.2) to validate (D2).

Taking the time derivative of (5.2) yields

$$\frac{d\Gamma}{dt} = 2\pi \int_0^\infty r \frac{d\omega_\theta}{dt} dr. \tag{D4}$$

Substituting (5.19) into (D4), we have

$$\frac{d\Gamma}{dt} = \frac{\pm A^+ k \Gamma^2(t)}{(1 - e^{-1}) \mathcal{G}(\Gamma, t)} \mathcal{Q}_I(t) \tag{D5}$$

with

$$\mathcal{Q}_I(t) = \frac{16\bar{v}}{k\dot{a}_0} \int_0^\infty \frac{1}{r^3} \left(1 - \exp\left(-\frac{r^2}{4\bar{v}t}\right)\right)^2 dr, \tag{D6}$$

where the integral of the viscous term \mathcal{V} over r vanishes. Thus, the only difference between (D2) and (D5) is due to the difference of \mathcal{Q}_T and \mathcal{Q}_I . We find that the temporal evolutions of \mathcal{Q}_T and \mathcal{Q}_I agree very well (not shown), where \mathcal{Q}_I is calculated by the Gauss–Legendre integral. Hence, the Taylor expansion in (D1) is still effective, and (D2) can be used as the model equation of circulations.

Appendix E. Comparison of models for spike and bubble growth rates in the RMI

We compare the present model (5.28) of spike and bubble growth rates in the RMI with several existing ones listed below.

- (i) The model suggested by Zhang & Sohn (1997, 1999):

$$\dot{a}_{s/b}(t) = \dot{a}(t) \pm \frac{\lambda_3 k \dot{a}_0^2 t}{1 + \lambda_4 \lambda_3^{-1} k^2 \dot{a}_0 a_0^+ t + \left[(\lambda_4 \lambda_3^{-1} k a_0^+)^2 + \lambda_5 \lambda_3^{-1} \right] (k \dot{a}_0 t)^2} \tag{E1}$$

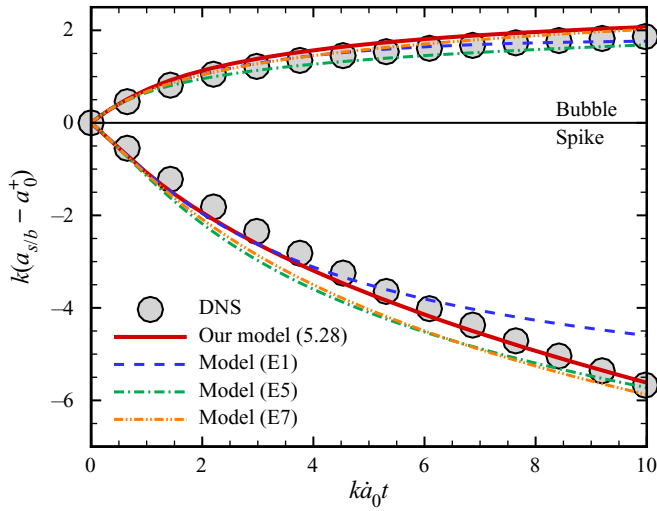


Figure 20. Comparison of the scaled spike/bubble amplitude calculated from the present DNS of the RMI at $A = 0.67$, the present model (5.28) and existing models.

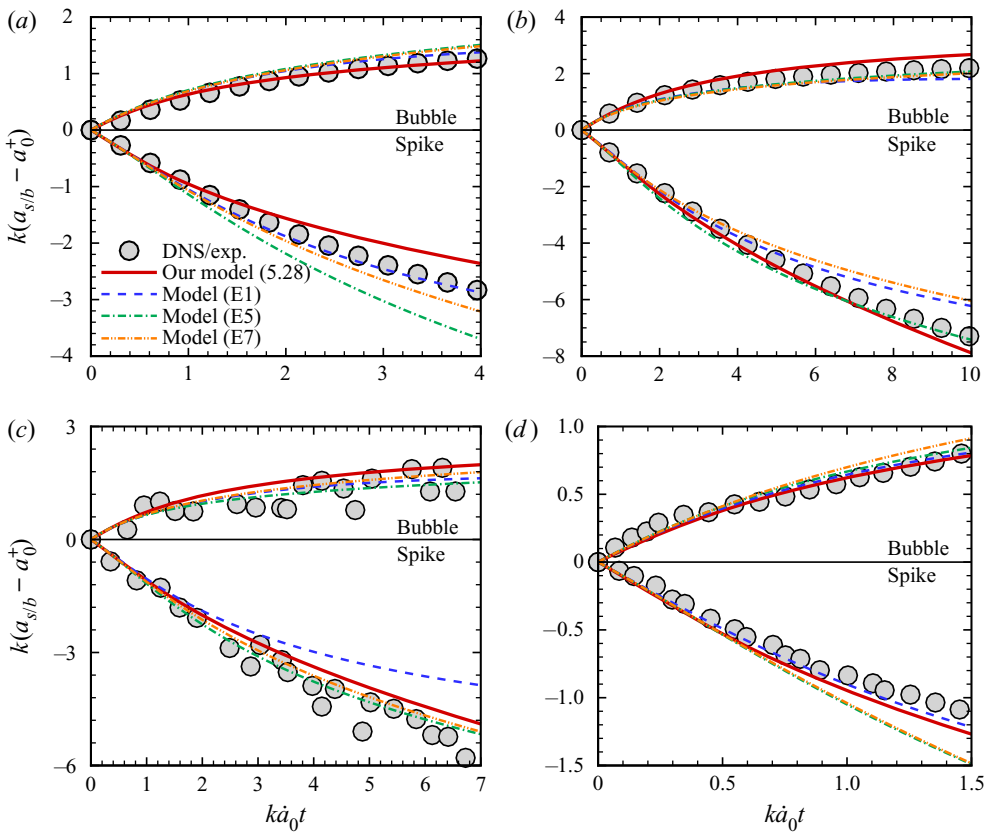


Figure 21. Comparison of the scaled spike/bubble amplitude calculated from the present model (5.28) and existing models, along with the data from (a) DNS of Latini *et al.* (2007), (b) DNS of Long *et al.* (2009), (c) experiment of Jacobs & Krivets (2005) and (d) experiment of Liang *et al.* (2019).

with

$$\dot{\tilde{a}}(t) = \frac{\dot{a}_0}{1 + \lambda_1 k^2 \dot{a}_0 a_0^+ t + \max\{0, (\lambda_1 k a_0^+)^2 - \lambda_2\} (k \dot{a}_0 t)^2}. \quad (\text{E2})$$

The parameters

$$\lambda_1 = 1, \quad \lambda_2 = (A^+)^2 - 0.5, \quad \lambda_3 = A^+, \quad \lambda_4 = 2A^+, \quad \lambda_5 = \frac{4}{3}A^+ \left[1 - (A^+)^2\right], \quad (\text{E3a-e})$$

are for the two-dimensional RMI, and

$$\left. \begin{aligned} \lambda_1 &= 0.088866(A^+)^2 + 0.455671, & \lambda_2 &= 0.391357(A^+)^2 - 0.227835, \\ \lambda_3 &= 0.01221(A^+)^3 + 0.69844A^+, & \lambda_4 &= 0.07035(A^+)^3 + 0.56513A^+, \\ \lambda_5 &= -0.30253(A^+)^3 + 0.38270A^+, \end{aligned} \right\} \quad (\text{E4})$$

are for the three-dimensional RMI.

(ii) The model suggested by Sadot *et al.* (1998):

$$\dot{a}_{s/b}(t) = \frac{\dot{a}_0 (1 + k \dot{a}_0 t)}{1 + (1 \mp A^+) k \dot{a}_0 t + F_{s/b} (k \dot{a}_0 t)^2} \quad (\text{E5})$$

with

$$F_{s/b} = \begin{cases} \frac{1 \mp A^+}{1 + A^+}, & A^+ \leq 0.5, \\ 1.5 \frac{1 \mp A^+}{1 + A^+}, & A^+ > 0.5. \end{cases} \quad (\text{E6})$$

(iii) The model suggested by Dimonte & Ramaprabhu (2010):

$$\dot{a}_{s/b}(t) = \frac{\dot{a}_0 [1 + (1 \pm A^+) k \dot{a}_0 t]}{1 + C_{s/b} k \dot{a}_0 t + D_{s/b} (k \dot{a}_0 t)^2} \quad (\text{E7})$$

with

$$C_{s/b} = \frac{4.5 \mp A^+ (2 \pm A^+) k a_0}{4} \quad \text{and} \quad D_{s/b} = 1 \mp A^+. \quad (\text{E8})$$

The model predictions of the scaled amplitude variation in the present DNS at $A = 0.67$ are compared in figure 20. We observe that all the models can predict the nonlinear growth of spikes and bubbles, and the present model (5.28) gives the overall best prediction. The model comparisons for other DNS and experimental series in the literature are shown in figure 21. In general, the predictions from the present model are comparable to or slightly better than the others.

REFERENCES

- AGLITSKIY, Y., *et al.* 2010 Basic hydrodynamics of Richtmyer–Meshkov-type growth and oscillations in the inertial confinement fusion-relevant conditions. *Phil. Trans. R. Soc. Lond. A* **368**, 1739–1768.
- ALMGREN, A.S., BELL, J.B., RENDLEMAN, C.A. & ZINGALE, M. 2006 Low Mach number modeling of type Ia supernovae. I. *Hydrodyn. Astrophys. J.* **637**, 922–936.
- ALON, U., HECHT, J., OFER, D. & SHVARTS, D. 1995 Power laws and similarity of Rayleigh–Taylor and Richtmyer–Meshkov mixing fronts at all density ratios. *Phys. Rev. Lett.* **74**, 534.
- ARNETT, D. 2000 The role of mixing in astrophysics. *Astrophys. J. Suppl.* **127**, 213.

- ARNETT, W.D., BAHCALL, J.N., KIRSHNER, R.P. & WOOSLEY, S.E. 1989 Supernova 1987A. *Annu. Rev. Astron. Astrophys.* **27**, 629–700.
- BRISCOE, M.G. & KOVITZ, A.A. 1968 Experimental and theoretical study of the stability of plane shock waves reflected normally from perturbed flat walls. *J. Fluid Mech.* **31**, 529–546.
- BROUILLETTE, M. 2002 The Richtmyer–Meshkov instability. *Annu. Rev. Fluid Mech.* **34**, 445–468.
- CARLÈS, P. & POPINET, S. 2002 The effect of viscosity, surface tension and non-linearity on Richtmyer–Meshkov instability. *Eur. J. Mech. B/Fluids* **21**, 511–526.
- CHAPMAN, S. & COWLING, T.G. 1990 *The Mathematical Theory of Non-Uniform Gases: An Account of the Kinetic Theory of Viscosity*. Cambridge University Press.
- CHAPMAN, P.R. & JACOBS, J.W. 2006 Experiments on the three-dimensional incompressible Richtmyer–Meshkov instability. *Phys. Fluids* **18**, 074101.
- COOK, A.W. 2009 Enthalpy diffusion in multicomponent flows. *Phys. Fluids* **21**, 055109.
- COURANT, R. & FRIEDRICHS, K.O. 1999 *Supersonic Flow and Shock Waves*. Springer.
- DIMONTE, G. & RAMAPRABHU, P. 2010 Simulations and model of the nonlinear Richtmyer–Meshkov instability. *Phys. Fluids* **22**, 014104.
- EVANS, L.C. 1998 *Partial Differential Equations*. American Mathematical Society.
- FRALEY, G. 1986 Rayleigh–Taylor stability for a normal shock wave-density discontinuity interaction. *Phys. Fluids* **29**, 376–386.
- FUKUMOTO, Y. & KAPLANSKI, F. 2008 Global time evolution of an axisymmetric vortex ring at low Reynolds numbers. *Phys. Fluids* **20**, 053103.
- FUKUMOTO, Y. & MOFFATT, H.K. 2008 Kinematic variational principle for motion of vortex rings. *Physica D* **237**, 2210–2217.
- GONCHAROV, V.N. 1999 Theory of the ablative Richtmyer–Meshkov instability. *Phys. Rev. Lett.* **82**, 2091.
- GOTTLIEB, S. & SHU, C.-W. 1998 Total variation diminishing Runge–Kutta schemes. *Maths Comput.* **67**, 73–85.
- GRAVES, R.E. & ARGROW, B.M. 1999 Bulk viscosity: past to present. *J. Thermophys. Heat Transfer* **13**, 337–342.
- GUPTA, S., ZHANG, S. & ZABUSKY, N.J. 2003 Shock interaction with a heavy gas cylinder: emergence of vortex bilayers and vortex-accelerated baroclinic circulation generation. *Laser Part. Beams* **21**, 443–448.
- HAAN, S.W. 1991 Weakly nonlinear hydrodynamic instabilities in inertial fusion. *Phys. Fluids B* **3**, 2349–2355.
- HAHN, M., DRIKAKIS, D., YOUNGS, D.L. & WILLIAMS, R.J.R. 2011 Richtmyer–Meshkov turbulent mixing arising from an inclined material interface with realistic surface perturbations and reshocked flow. *Phys. Fluids* **23**, 046101.
- HAO, J., XIONG, S. & YANG, Y. 2019 Tracking vortex surfaces frozen in the virtual velocity in non-ideal flows. *J. Fluid Mech.* **863**, 513–544.
- HILL, D.J., PANTANO, C. & PULLIN, D.I. 2006 Large-eddy simulation and multiscale modelling of a Richtmyer–Meshkov instability with reshock. *J. Fluid Mech.* **557**, 29–61.
- ISHIZAKI, R., NISHIHARA, K., SAKAGAMI, H. & UESHIMA, Y. 1996 Instability of a contact surface driven by a nonuniform shock wave. *Phys. Rev. E* **53**, R5592.
- JACOBS, J.W. & KRIVETS, V.V. 2005 Experiments on the late-time development of single-mode Richtmyer–Meshkov instability. *Phys. Fluids* **17**, 034105.
- JACOBS, J.W. & SHEELEY, J.M. 1996 Experimental study of incompressible Richtmyer–Meshkov instability. *Phys. Fluids* **8**, 405–415.
- JIANG, G.S. & SHU, C.-W. 1996 Efficient implementation of weighted ENO schemes. *J. Comput. Phys.* **126**, 202–228.
- KAWAI, S. & LELE, S.K. 2008 Localized artificial diffusivity scheme for discontinuity capturing on curvilinear meshes. *J. Comput. Phys.* **227**, 9498–9526.
- KHOKHLOV, A.M., ORAN, E.S. & THOMAS, G.O. 1999 Numerical simulation of deflagration-to-detonation transition: the role of shock-flame interactions in turbulent flames. *Combust. Flame* **117**, 323–339.
- KOKKINAKIS, I.W., DRIKAKIS, D. & YOUNGS, D.L. 2019 Modeling of Rayleigh–Taylor mixing using single-fluid models. *Phys. Rev. E* **99**, 013104.
- KOTELNIKOV, A.D., RAY, J. & ZABUSKY, N.J. 2000 Vortex morphologies on reaccelerated interfaces: visualization, quantification and modeling of one-and two-mode compressible and incompressible environments. *Phys. Fluids* **12**, 3245–3264.
- LATINI, M., SCHILLING, O. & DON, W.S. 2007 High-resolution simulations and modeling of reshocked single-mode Richtmyer–Meshkov instability: comparison to experimental data and to amplitude growth model predictions. *Phys. Fluids* **19**, 024104.

- LIANG, Y., ZHAI, Z., DING, J. & LUO, X. 2019 Richtmyer–Meshkov instability on a quasi-single-mode interface. *J. Fluid Mech.* **872**, 729–751.
- LIKHACHEV, O.A. & JACOBS, J.W. 2005 A vortex model for Richtmyer–Meshkov instability accounting for finite Atwood number. *Phys. Fluids* **17**, 031704.
- LINDL, J.D., MCCRORY, R.L. & CAMPBELL, E.M. 1992 Progress toward ignition and burn propagation in inertial confinement fusion. *Phys. Today* **45**, 32–40.
- LIU, H. & XIAO, Z. 2016 Scale-to-scale energy transfer in mixing flow induced by the Richtmyer–Meshkov instability. *Phys. Rev. E* **93**, 053112.
- LOMBARDINI, M. & PULLIN, D.I. 2009 Small-amplitude perturbations in the three-dimensional cylindrical Richtmyer–Meshkov instability. *Phys. Fluids* **21**, 114103.
- LONG, C.C., KRIVETS, V.V., GREENOUGH, J.A. & JACOBS, J.W. 2009 Shock tube experiments and numerical simulation of the single-mode, three-dimensional Richtmyer–Meshkov instability. *Phys. Fluids* **21**, 114104.
- LUO, X., WANG, X. & SI, T. 2013 The Richtmyer–Meshkov instability of a three-dimensional air/SF₆ interface with a minimum-surface feature. *J. Fluid Mech.* **722**, R2.
- MEIRON, D. & MELOON, M. 1997 Richtmyer–Meshkov instability in compressible stratified fluids. In *Proceedings of the 6th International Workshop on the Physics of Compressible Turbulent Mixing, Marseille, France* (ed. G. Jourdan & L. Hovas), pp. 337–342. Institut Universitaire Thermiques Industriels, Marseille, France.
- MESHKOV, E.E. 1969 Instability of the interface of two gases accelerated by a shock wave. *Fluid Dyn.* **4**, 101–104.
- MIKAELIAN, K.O. 1993 Effect of viscosity on Rayleigh–Taylor and Richtmyer–Meshkov instabilities. *Phys. Rev. E* **47**, 375.
- MIKAELIAN, K.O. 2003 Explicit expressions for the evolution of single-mode Rayleigh–Taylor and Richtmyer–Meshkov instabilities at arbitrary Atwood numbers. *Phys. Rev. E* **67**, 026319.
- MORGAN, R.V., AURE, R., STOCKERO, J.D., GREENOUGH, J.A., CABOT, W., LIKHACHEV, O.A. & JACOBS, J.W. 2012 On the late-time growth of the two-dimensional Richtmyer–Meshkov instability in shock tube experiments. *J. Fluid Mech.* **712**, 354–383.
- MOVAHED, P. & JOHNSEN, E. 2013 A solution-adaptive method for efficient compressible multifluid simulations, with application to the Richtmyer–Meshkov instability. *J. Comput. Phys.* **239**, 166–186.
- NIEDERHAUS, C.E. & JACOBS, J.W. 2003 Experimental study of the Richtmyer–Meshkov instability of incompressible fluids. *J. Fluid Mech.* **485**, 243–277.
- NISHIHARA, K., WOUCHUK, J.G., MATSUOKA, C., ISHIZAKI, R. & ZHAKHOVSKY, V.V. 2010 Richtmyer–Meshkov instability: theory of linear and nonlinear evolution. *Phil. Trans. R. Soc. A* **368**, 1769–1807.
- OGGIAN, T., DRIKAKIS, D., YOUNGS, D.L. & WILLIAMS, R.J.R. 2015 Computing multi-mode shock-induced compressible turbulent mixing at late times. *J. Fluid Mech.* **779**, 411–431.
- OLSON, B.J. & LELE, S.K. 2013 A mechanism for unsteady separation in over-expanded nozzle flow. *Phys. Fluids* **25**, 239–249.
- ORTEGA, A., HILL, D.J., PULLIN, D.I. & MEIRON, D.I. 2010 Linearized Richtmyer–Meshkov flow analysis for impulsively accelerated incompressible solids. *Phys. Rev. E* **81**, 066305.
- PANTANO, C., DEITERDING, R., HILL, D.J. & PULLIN, D.I. 2007 A low numerical dissipation patch-based adaptive mesh refinement method for large-eddy simulation of compressible flows. *J. Comput. Phys.* **221**, 63–87.
- PENG, N. & YANG, Y. 2018 Effects of the Mach number on the evolution of vortex-surface fields in compressible Taylor–Green flows. *Phys. Rev. Fluids* **3**, 013401.
- PENG, G., ZABUSKY, N.J. & ZHANG, S. 2003 Vortex-accelerated secondary baroclinic vorticity deposition and late-intermediate time dynamics of a two-dimensional Richtmyer–Meshkov interface. *Phys. Fluids* **15**, 3730–3744.
- RAMSHAW, J.D. 1990 Self-consistent effective binary diffusion in multicomponent gas mixtures. *J. Non-Equilib. Thermodyn.* **15**, 295–300.
- RASMUS, A.M., *et al.* 2018 Shock-driven discrete vortex evolution on a high-Atwood number oblique interface. *Phys. Plasma* **25**, 032119.
- REID, R.C., PRANSUITZ, J.M. & POLING, B.E. 1987 *The Properties of Gases and Liquids*. McGraw-Hill.
- REINAUD, J., JOLY, L. & CHASSAING, P. 2000 The baroclinic secondary instability of the two-dimensional shear layer. *Phys. Fluids* **12**, 2489–2505.
- RICHTMYER, R.D. 1960 Taylor instability in shock acceleration of compressible fluids. *Commun. Pure Appl. Maths* **13**, 297–319.

- SADOT, O., EREZ, L., ALON, U., ORON, D., LEVIN, L.A., EREZ, G., BEN-DOR, G. & SHVARTS, D. 1998 Study of nonlinear evolution of single-mode and two-bubble interaction under Richtmyer–Meshkov instability. *Phys. Rev. Lett.* **80**, 1654.
- SAFFMAN, P.G. 1970 The velocity of viscous vortex rings. *Stud. Appl. Maths* **49**, 371–380.
- SAMTANEY, R., RAY, J. & ZABUSKY, N.J. 1998 Baroclinic circulation generation on shock accelerated slow/fast gas interfaces. *Phys. Fluids* **10**, 1217–1230.
- SAMTANEY, R. & ZABUSKY, N.J. 1994 Circulation deposition on shock-accelerated planar and curved density-stratified interfaces: models and scaling laws. *J. Fluid Mech.* **269**, 45–78.
- SHANKAR, S.K., KAWAI, S. & LELE, S.K. 2011 Two-dimensional viscous flow simulation of a shock accelerated heavy gas cylinder. *Phys. Fluids* **23**, 131.
- SOHN, S.-I. 2004 Vortex model and simulations for Rayleigh–Taylor and Richtmyer–Meshkov instabilities. *Phys. Rev. E* **69**, 036703.
- SOHN, S.-I. 2009 Effects of surface tension and viscosity on the growth rates of Rayleigh–Taylor and Richtmyer–Meshkov instabilities. *Phys. Rev. E* **80**, 055302.
- SOTERIOU, M.C. & GHONIEM, A.F. 1995 Effects of the free-stream density ratio on free and forced spatially developing shear layers. *Phys. Fluids* **7**, 2036–2051.
- STAQUET, C. 1995 Two-dimensional secondary instabilities in a strongly stratified shear layer. *J. Fluid Mech.* **296**, 73–126.
- TACCETTI, J.M., BATHA, S.H., FINCKE, J.R., DELAMATER, N.D., LANIER, N.E., MAGELSSSEN, G.R., HUECKSTAEDT, R.M., ROTHMAN, S.D., HORSFIELD, C.J. & PARKER, K.W. 2005 Richtmyer–Meshkov instability reshock experiments using laser-driven double-cylinder implosions. *Astrophys. Space Sci.* **298**, 327–331.
- THORNER, B., DRIKAKIS, D., YOUNGS, D.L. & WILLIAMS, R.J.R. 2010 The influence of initial conditions on turbulent mixing due to Richtmyer–Meshkov instability. *J. Fluid Mech.* **654**, 99–139.
- THORNER, B., DRIKAKIS, D., YOUNGS, D.L. & WILLIAMS, R.J.R. 2011 Growth of a Richtmyer–Meshkov turbulent layer after reshock. *Phys. Fluids* **23**, 095107.
- THORNER, B., DRIKAKIS, D., YOUNGS, D.L. & WILLIAMS, R.J.R. 2012 Physics of the single-shocked and reshocked Richtmyer–Meshkov instability. *J. Turbul.* **13**, 1–17.
- TRITSCHLER, V.K., ZUBEL, M., HICKEL, S. & ADAMS, N.A. 2014 Evolution of length scales and statistics of Richtmyer–Meshkov instability from direct numerical simulations. *Phys. Rev. E* **90**, 063001.
- TUNG, C. & TING, L. 1967 Motion and decay of a vortex ring. *Phys. Fluids* **10**, 901–910.
- VANDENBOOMGAERDE, M., GAUTHIER, S. & MÜGLER, C. 2002 Nonlinear regime of a multimode Richtmyer–Meshkov instability: a simplified perturbation theory. *Phys. Fluids* **14**, 1111–1122.
- VELIKOVICH, A.L., DAHLBURG, J.P., SCHMITT, A.J., GARDNER, J.H., PHILLIPS, L., COCHRAN, F.L., CHONG, Y.K., DIMONTE, G. & METZLER, N. 2000 Richtmyer–Meshkov-like instabilities and early-time perturbation growth in laser targets and Z-pinch loads. *Phys. Plasmas* **7**, 1662–1671.
- VELIKOVICH, A.L., HERRMANN, M. & ABARZHI, S.I. 2014 Perturbation theory and numerical modelling of weakly and moderately nonlinear dynamics of the incompressible Richtmyer–Meshkov instability. *J. Fluid Mech.* **751**, 432–479.
- VOROBIEFF, P., TOMKINS, C., KUMAR, S., GOODENOUGH, C., MOHAMED, N.G. & BENJAMIN, R.F. 2004 Secondary instabilities in shock-induced transition to turbulence. *Adv. Fluid Mech.* **45**, 139–148.
- WOCHUK, J.G. 2001 Growth rate of the linear Richtmyer–Meshkov instability when a shock is reflected. *Phys. Rev. E* **63**, 056303.
- WOCHUK, J.G. & NISHIHARA, K. 1997 Asymptotic growth in the linear Richtmyer–Meshkov instability. *Phys. Plasmas* **4**, 1028–1038.
- WU, J., LIU, H. & XIAO, Z. 2019 A numerical investigation of Richtmyer–Meshkov instability in spherical geometry. *Adv. Appl. Maths Mech.* **11**, 583–597.
- XIONG, S. & YANG, Y. 2019a Construction of knotted vortex tubes with the writhe-dependent helicity. *Phys. Fluids* **31**, 047101.
- XIONG, S. & YANG, Y. 2019b Identifying the tangle of vortex tubes in homogeneous isotropic turbulence. *J. Fluid Mech.* **874**, 952–978.
- YANG, J., KUBOTA, T. & ZUKOSKI, E.E. 1993 Applications of shock-induced mixing to supersonic combustion. *AIAA J.* **31**, 854–862.
- YANG, Y. & PULLIN, D.I. 2010 On Lagrangian and vortex-surface fields for flows with Taylor–Green and Kida–Pelz initial conditions. *J. Fluid Mech.* **661**, 446–481.
- YANG, Y. & PULLIN, D.I. 2011 Evolution of vortex-surface fields in viscous Taylor–Green and Kida–Pelz flows. *J. Fluid Mech.* **685**, 146–164.
- YANG, Y., ZHANG, Q. & SHARP, D.H. 1994 Small amplitude theory of Richtmyer–Meshkov instability. *Phys. Fluids* **6**, 1856–1873.

- ZABUSKY, N.J. 1999 Vortex paradigm for accelerated inhomogeneous flows: visiometrics for the Rayleigh–Taylor and Richtmyer–Meshkov environments. *Annu. Rev. Fluid Mech.* **31**, 495–536.
- ZABUSKY, N.J., KOTELNIKOV, A.D., GULAK, Y. & PENG, G. 2003 Amplitude growth rate of a Richtmyer–Meshkov unstable two-dimensional interface to intermediate times. *J. Fluid Mech.* **475**, 147–162.
- ZABUSKY, N.J. & ZENG, S.M. 1998 Shock cavity implosion morphologies and vortical projectile generation in axisymmetric shock-spherical fast/slow bubble interactions. *J. Fluid Mech.* **362**, 327–346.
- ZABUSKY, N.J. & ZHANG, S. 2002 Shock-planar curtain interactions in two dimensions: emergence of vortex double layers, vortex projectiles, and decaying stratified turbulence. *Phys. Fluids* **14**, 419–422.
- ZAIDEL, P.M. 1960 Shock wave from a slightly curved piston. *Z. Angew. Math. Mech.* **24**, 316–327.
- ZHANG, S., PENG, G. & ZABUSKY, N.J. 2005 Vortex dynamics and baroclinically forced inhomogeneous turbulence for shock-planar heavy curtain interactions. *J. Turbul.* **6**, N3.
- ZHANG, Q. & SOHN, S.-I. 1996 An analytical nonlinear theory of Richtmyer–Meshkov instability. *Phys. Lett. A* **212**, 149–155.
- ZHANG, Q. & SOHN, S.-I. 1997 Nonlinear theory of unstable fluid mixing driven by shock wave. *Phys. Fluids* **9**, 1106–1124.
- ZHANG, Q. & SOHN, S.-I. 1999 Quantitative theory of Richtmyer–Meshkov instability in three dimensions. *Z. Angew. Math. Phys.* **50**, 1–46.
- ZHANG, S. & ZABUSKY, N.J. 2003 Shock-planar curtain interactions: strong secondary baroclinic deposition and emergence of vortex projectiles and late-time inhomogeneous turbulence. *Laser Part. Beams* **21**, 463–470.
- ZHANG, S., ZABUSKY, N.J., PENG, G. & GUPTA, S. 2004 Shock gaseous cylinder interactions: dynamically validated initial conditions provide excellent agreement between experiments and numerical simulations to late-intermediate time. *Phys. Fluids* **16**, 1203–1216.
- ZHAO, Y., XIONG, S., YANG, Y. & CHEN, S. 2018 Sinuous distortion of vortex surfaces in the lateral growth of turbulent spots. *Phys. Rev. Fluids* **3**, 074701.
- ZHAO, Y., YANG, Y. & CHEN, S. 2016 Vortex reconnection in the late transition in channel flow. *J. Fluid Mech.* **802**, R4.
- ZHOU, Y. 2001 A scaling analysis of turbulent flows driven by Rayleigh–Taylor and Richtmyer–Meshkov instabilities. *Phys. Fluids* **13**, 538–543.
- ZHOU, Y. 2017*a* Rayleigh–Taylor and Richtmyer–Meshkov instability induced flow, turbulence, and mixing. I. *Phys. Rep.* **720a**, 1–136.
- ZHOU, Y. 2017*b* Rayleigh–Taylor and Richtmyer–Meshkov instability induced flow, turbulence, and mixing. II. *Phys. Rep.* **723**, 1–160.
- ZHOU, H., YOU, J., XIONG, S., YANG, Y., THÉVENIN, D. & CHEN, S. 2019 Interactions between the premixed flame front and the three-dimensional Taylor–Green vortex. *Proc. Combust. Inst.* **37**, 2461–2468.